AIAA JOURNAL
Vol. 46, No. 11, November 2008

Turbulence Within a Turbomachine Rotor Wake Subject to Nonuniform Contraction

Francesco Soranna,* Yi-Chih Chow,† Oguz Uzol,‡ and Joseph Katz§
The Johns Hopkins University, Baltimore, Maryland 21218

DOI: 10.2514/1.31079

The flow and turbulence in a rotor near wake located within a nonuniform field, generated by a row of inlet guide vanes, are investigated experimentally in a refractive-index-matched facility that provides unobstructed view of the entire flowfield. Stereoscopic particle image velocimetry measurements, performed in closely spaced radial planes, enable measurements of all the components of the phase-averaged strain rate, Reynolds stress, and triple correlation tensors. The rotor wake is bent and compressed as a result of exposure to regions with high axial momentum ("jets"), which fill the gaps between inlet guide vanes wakes. As the rotor wake propagates away from the blade, this process of bending and compression by the jets leads to formation of distinct wake kinks containing regions of high turbulence (turbulent "hot spots"). We focus on an early stage of hot-spot formation. On the suction side of the wake, compression by a jet increases turbulence production, causing nonuniform and asymmetric distribution of Reynolds stresses. In a curvilinear coordinate system aligned with the wake centerline, all the Reynolds stresses are higher on the suction side of the wake where the decay rate of turbulence is much slower than that expected in wakes. The production rate of streamwise stress is dominated by interactions of the shear stress with the cross-stream gradients of the phase-averaged streamwise velocity. The latter also interact with the cross-stream stress to cause high production of shear stress, especially on the suction side. The locations of peak streamwise and shear stresses are consistent with those of the corresponding production rates. The similar locations of peak streamwise and cross-stream stresses, together with low production rate of the latter, suggest a significant contribution by intercomponent transfer from the streamwise to the cross-stream stress. The effects of streamwise curvature and rotation on the evolution of turbulent stresses are marginal. The paper also provides distributions of advection by phase-averaged flow and turbulent diffusion components. The diffusion terms oppose the peaks of production rates, but also have high values along the perimeter of the wake. We compare the distribution of diffusion of turbulent kinetic energy to a model based on the gradient-diffusion hypothesis. The model predicts the diffusion peak that opposes the production rate maximum quite well, but underpredicts the diffusion along the perimeter of the wake and overpredicts it near the wake center.

Introduction

THE flow within multistage turbomachines contains multiple blade wakes that interact with each other and with blades located downstream. Unlike isolated wakes in uniform flows, turbomachinery wakes are subjected to unsteady and spatially nonuniform strain fields generated by upstream blades and wakes, flow curvature, and Coriolis and centrifugal forces. Consequently, the wakes deform and the structure of the turbulence within them is modified.

In recent papers, Chow et al. [1,2] describe the complex flow within the wake shed by a rotor blade, located downstream of a row of inlet guide vanes (IGVs). The data are obtained in a refractive-index-matched facility that provides an unobstructed view of the entire flowfield. One of the several phenomena observed in their studies is formation of a series of wake kinks and turbulent hot spots caused by the nonuniform flow generated by upstream wakes. These turbulent hot spots occur in cold flow and should not be confused with temperature hot spots seen, for example, in vortex streets behind cylinders (Kurosaka et al. [3]) and in wakes of turbine blades at high subsonic Mach number (Sieverding et al. [4]), which result from energy separation (Eckert and Weise [5]). To illustrate the turbulent hot spots, Fig. 1 shows distributions of phase-averaged spanwise vorticity $\overline{\omega_z}$ and in-plane components of turbulent kinetic energy k in the turbomachine rotor wake of Chow et al. [2] (these measurements were two-dimensional). The hot spot is located in the region where the wake is kinked, centered at about $(x/c, y/c) = (-0.3, -0.62)$, where c is the chord length of the rotor blade, and is characterized by "discontinuity" in vorticity distribution and elevated turbulent kinetic energy. The peak in turbulent kinetic energy is shifted from the peak in vorticity.

Sample particle image velocimetry (PIV) planes recorded at other spanwise locations (not shown), indicate that hot-spot formation occurs at all planes except for the tip region, where the tip vortex dominates, and very near the hub due to the presence of secondary flows there. Furthermore, multiple hot spots can be identified within the same rotor wake, due to periodicity of the external flow nonuniformities. With time, the turbulence within the hot spots diffuses and, consequently, the turbulent intensity diminishes. Chow et al. [1] also show that formation of turbulent hot spots occurs in a different turbomachine setup and over several rotor phases of an entire rotor revolution cycle. The process leading to formation of such a complex structure is the motivation for the present study.

To elucidate this process, we start by examining the flowfield at a lower magnification. Figure 2 presents lower resolution distributions of k and phase-averaged axial velocity $\overline{U}$ at 50% of the rotor span. Data show the same rotor wake as that analyzed by Chow et al. [2]

Received 16 March 2007; revision received 29 December 2007; accepted for publication 9 April 2008.

*Graduate Research Assistant, Mechanical Engineering, 223 Latrobe Hall; currently Aeromechanics Engineer, GE-Energy, 300 Garlington Road, Greenville, SC 29615. Member AIAA.

†Graduate Research Assistant, Mechanical Engineering; currently Assistant Professor, Department of Systems Engineering and Naval Architecture, National Taiwan Ocean University 2, Pei-Ning Road, Keelung 20224, Taiwan, Republic of China. Member AIAA.

‡Postdoctoral Fellow, Mechanical Engineering; currently Assistant Professor, Department of Aerospace Engineering, Middle East Technical University, ODTU Havacilik ve Uzay Muh Bol, 06531 Ankara, Turkey. Member AIAA.

§William F. Ward Sr. Distinguished Professor of Mechanical Engineering, Mechanical Engineering, 117 Latrobe Hall. Member AIAA.

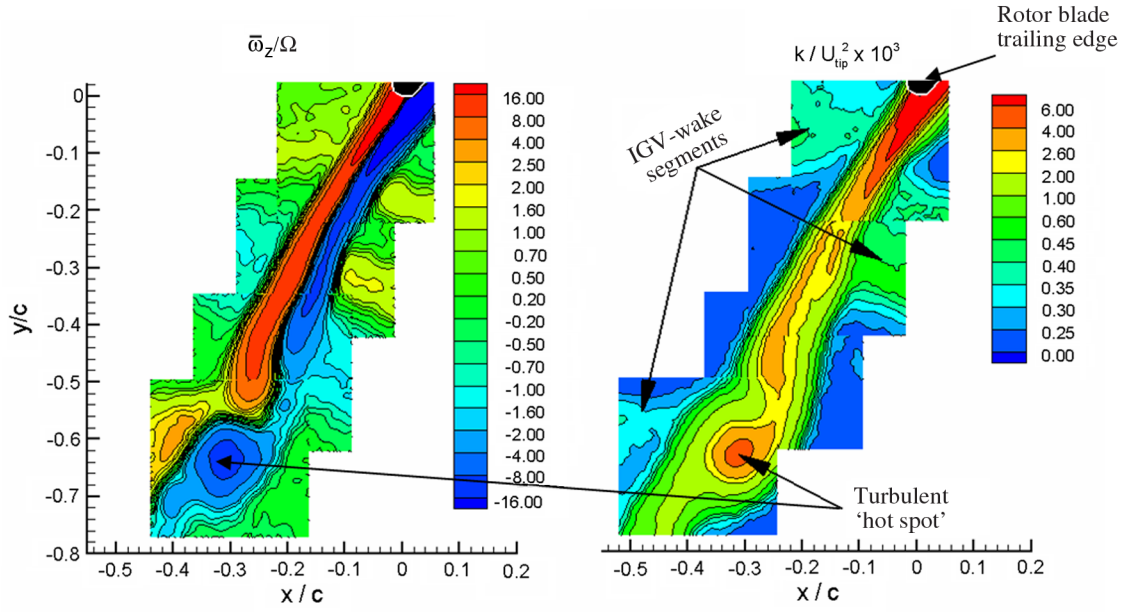

Fig. 1 Distribution of a) phase-averaged spanwise-vorticity normalized by rotational speed and b) in-plane component of turbulent kinetic energy in a wake of a rotor blade subject to nonuniform flow generated by upstream IGV wakes (Chow et al. [2]).

and in this paper, but at a different rotor phase. These data were recorded during earlier stages of this project and their accuracy is lower in comparison to that of Fig. 1, due to lower resolution and smaller number of instantaneous realization (100) used for obtaining the phase-averaged statistics. However, the larger field of view is instructive. Either side of the rotor wake is exposed to regions of high axial momentum that "fill" the gaps between the low-momentum IGV wakes. We refer to these regions as jets. Based on the k distribution, we mark the edges of the rotor wakes (lines a–d), as well as the boundaries between IGV-wake segments and jets (lines e–i). Notice the presence of two hot spots, with the one on the top left corner generated within the rotor wake of a previous blade in the same row. Turbulence is high within the IGV and rotor wakes, as well as in the hot spots, but drops to very low levels within the jets. The axial velocity is high in the jet regions and low within the wakes. Chopped IGV-wake segments are offset from each other across the rotor wake because of differences in advection speeds on the suction and pressure sides of the rotor blade. Consequently, the locations of the jets are also shifted across the rotor wake. These jets bend and squeeze the rotor wakes. Compression of the contour lines of $\overline{U}$ evident in the region of peak jet velocity, implies a local increase of velocity gradients. As a result, and shown in detail later, turbulence production also increases.

In an attempt to understand the process leading to formation of rotor-wake hot spots, we have examined the extensive literature on curved wakes. One of the common observations has been that curvature increases the turbulence in the inner side of the wake and decreases it in the outer side. Some of these effects have been explained in terms of variation in the production rate across the wake due to the effect of wake curvature (Weygandt and Metha [6]). Various means have been used to generate the wake and to bend them. For example, wakes of isolated and cascade airfoils at incidence have been studied by Hah and Lakshminarayana [7] and Raj and Lakshminarayana [8]. The first study shows the tendency of the turbulent kinetic energy and the shear stress to increase in the inner side of the wake and decrease in the outer side. In the second

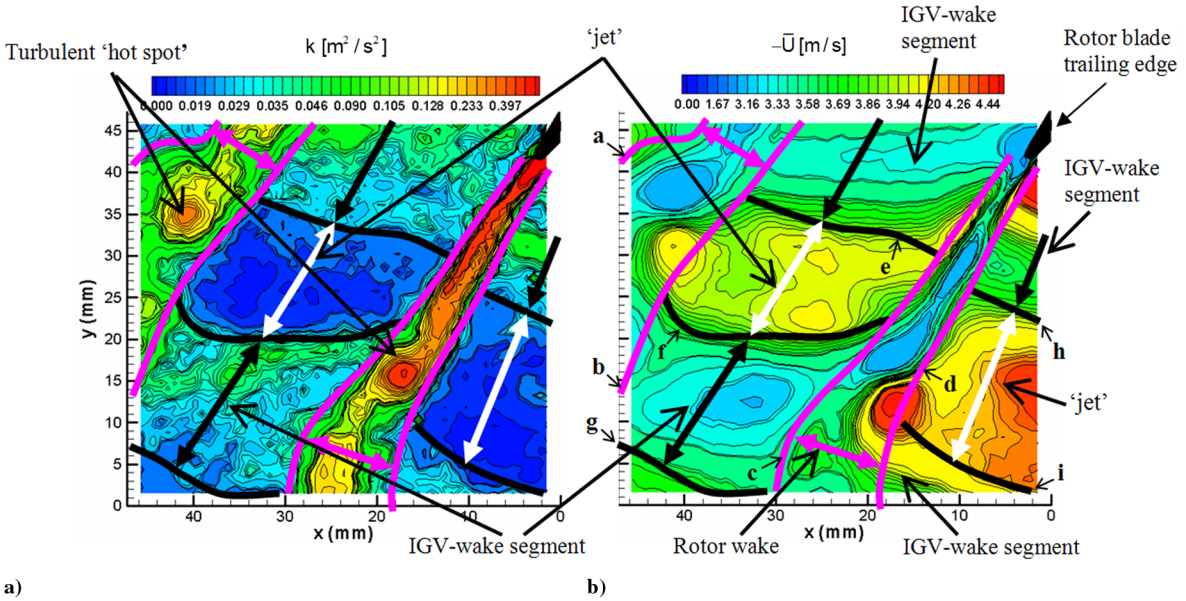

Fig. 2 Sample, low-magnification distributions of in-plane component of turbulent kinetic energy and a) phase-averaged axial velocity b) in the rotor wake of Fig. 1 at a different rotor phase, showing multiple turbulent hot spots and flow nonuniformities at 50% of rotor span.

study, the peaks of the streamwise and cross-stream Reynolds stresses are slightly shifted toward the outer side of the wake. However, these trends are attributed to the effect of previous history of the flow rather than to curvature. Ramjee et al. [9] observed an increase in streamwise velocity fluctuations in the inner side of an airfoil-wake in a curved duct. Investigations on the wakes behind cylinders (e.g., Koyama [10], Ramjee and Neelakandan [11], Schobeiri et al. [12]) and splitter plates (Weygandt and Metha [6]) in curved channels confirm the enhancement of various components of the Reynolds stress tensor, especially the shear stress, in the inner side of the wake.

High sensitivity of the Reynolds shear stress to wake curvature was also observed when streamwise curvature is combined with pressure gradients. These conditions have been achieved by bending a cylinder wake with a back plate (Savill [13]) and a thin wire wake with an airfoil-like plate (Nakayama [14]). Other approaches consisted of varying the cross sections of a curved channel containing a cylinder wake (John and Schobeiri [15]) and placing a plate in a diverging channel (Starke et al. [16]). As shown later in this paper, curvature effects are minor compared with other phenomena, in particular, the previously mentioned compression of the wake on the suction side by the jets, which substantially increases the shear production.

To examine the process leading to formation of the hot spots, we focus on an earlier stage of the wake compared to the one studied by Chow et al. [2]. We start by presenting data on the structure of the rotor wake in Cartesian coordinates and show the spatially nonuniform and highly anisotropic distribution of Reynolds stresses. To explain these trends, we reexamine the data and the corresponding production rate components in a curvilinear coordinate system aligned with the wake centerline. We show that the distribution of Reynolds stresses is consistent with the spatially nonuniform distribution of turbulence production rate and identify specific contributors. We provide evidence that spatial variations in shear velocity gradients, caused by squeezing of the rotor wake by the previously described jets, dominate the nonuniform turbulence production. We also look at the distribution of the turbulent diffusion of turbulent kinetic energy and compare it to trends predicted by a model based on the gradient-diffusion hypothesis. In spite of substantial flow nonuniformities, there is agreement in trends in most of the wake. Before presenting results, the facility and experimental setup are described in the following section.

Experimental Setup and Procedures

Facility

The axial turbomachine test facility is constructed to facilitate unobstructed, detailed PIV measurements within an entire stage, achieved by matching the optical refractive index of the blades with that of the fluid. As described in previous publications (Uzol et al. [17,18], Chow et al. [1]), the rotor and stator blade rows are made of transparent acrylic and the fluid is a concentrated solution of sodium iodide in water (62–64% by weight). This fluid has a specific gravity of 1.8 and a kinematic viscosity of 1.1×10^{-6} m^2/s, that is, very close to that of water.

As shown in Fig. 3a, in the setup used in the present study, the two-stage axial turbomachine has four blade rows. The first-stage rotor is directly driven by a 25-hp, rim-driven motor, preventing the need for a long shaft. The two rotors are connected by a common shaft supported by precision bearings. The first stage consists of a rotor followed by a stator, whereas the second stage consists of a stator (IGV) followed by a rotor. A 10-mm-long honeycomb with 1.58-mm-diam openings is installed downstream of the first stage to reduce the effect of wakes and secondary structures generated by the first stage. The gap between the honeycomb and the second-stage stator is 22 times the honeycomb opening, allowing individual honeycomb wakes to merge, as verified in previous measurements. All the present measurements are performed at a condition close to the design point of this turbomachine at a rotational speed $\Omega = 500$ rpm. The corresponding Reynolds number based on the tip speed and the chord of the rotor blade is 370,000.

Some geometric details of the IGV and the rotor blades are summarized in Table 1. More information about the facility can be found in Uzol et al. [18] and Chow et al. [1].

Stereoscopic Particle Imaging Velocimetry Setup and Experimental Procedure

Stereoscopic-PIV measurements are performed at midspan within a region that extends from the rotor blade trailing edge to about 30% of the chord length c below the trailing edge (see Fig. 3b). The light source is a 120 mJ/pulse Nd-YAG laser, whose beam is expanded to generate a 1-mm-thick light sheet. The flow is seeded using 20% silver-coated, hollow glass spheres, which have a mean diameter of 13 μm and an average specific gravity of 1.6, that is, slightly below that of the working fluid. The images are recorded by two Kodak ES4.0, 2048×2048 pixels^2, 8-bit digital cameras, mounted on a traversing platform. The lenses are rotated to obtain a 30 deg viewing angle with respect to the radial z direction. The charge-coupled device arrays of both cameras are further rotated by another 14 deg to satisfy the Scheimpflug condition (Prasad and Jensen [19]). The overlap region viewed by the two cameras corresponds to an area of 27.5×22.5 mm (0.55×0.45 c). To minimize optical distortions, an acrylic prism filled with a refractive-index-matched fluid is attached to the facility window, with its windows aligned with the camera lenses. The prism's position on the window can be shifted for observing any part of the blade passage.

The laser and the cameras are synchronized with the orientation of the rotor, using a shaft encoder that feeds a signal to a controller containing adjustable delay generators. All the data presented in this paper are recorded at the same phase. Data processing includes image filtering and enhancement, followed by two-dimensional cross-correlation analysis using in-house developed software and procedures (Uzol et al. [17], Roth et al. [20], Roth and Katz [21]). Combining the two two-dimensional vector maps, a planar distribution of all three velocity components is achieved using the Flow Manager, three-dimensional PIV software provided by Dantec, Inc. This software is integrated with our in-house PIV data analysis tools.

Calibration of the stereoscopic setup is performed outside of the test section due to space limitations. During the calibration, the prism is attached to an acrylic box filled with a refractive-index-matched fluid. The calibration target is inserted in the box, and is precisely positioned at locations that correspond to the measurement planes. Stereoscopic images of the target are obtained at five different planes within the 1 mm laser sheet thickness, for each spanwise position. They are fed to the Dantec software, which generates the transformation matrix needed for computing the three velocity components.

The measurements discussed in this paper are performed in 10 spanwise planes located between $z/(r_{\text{tip}} - r_{\text{hub}}) = 0.50 - 0.55$ (i.e., 50–55% of the span), where z is oriented in the radial direction (Fig. 3a), with $z = 0$ located at the hub, and r_{tip} and r_{hub} indicate radii of the blade tip and the hub, respectively. These 10 radial planes are separated by 0.25 mm (0.5% of the chord length). The in-plane vector spacings are 0.5 and 0.425 mm in the x (axial) and y (lateral, almost circumferential) directions, respectively. The difference is caused by the stereoscopic observations. Most of the analysis presented in this paper is shown at one specific spanwise plane. However, no two-dimensional assumptions are made in the calculation of vorticity and strain fields, as well as the terms in the transport equations for turbulent kinetic energy and Reynolds stresses. All contributing three-dimensional terms are included.

To obtain converged turbulence statistics, we record 1000 velocity distributions in each plane. The in-plane velocity derivatives are calculated using second-order central differencing within the sample area and first-order forward/backward differencing along the boundaries. Second-order polynomials are fitted to the data points in the z direction at each grid point, while calculating the z (radial) derivatives of velocity, to avoid the effect of jitter resulting from matching data in different planes. The phase-averaged velocity vector and Reynolds stress tensor components are calculated using

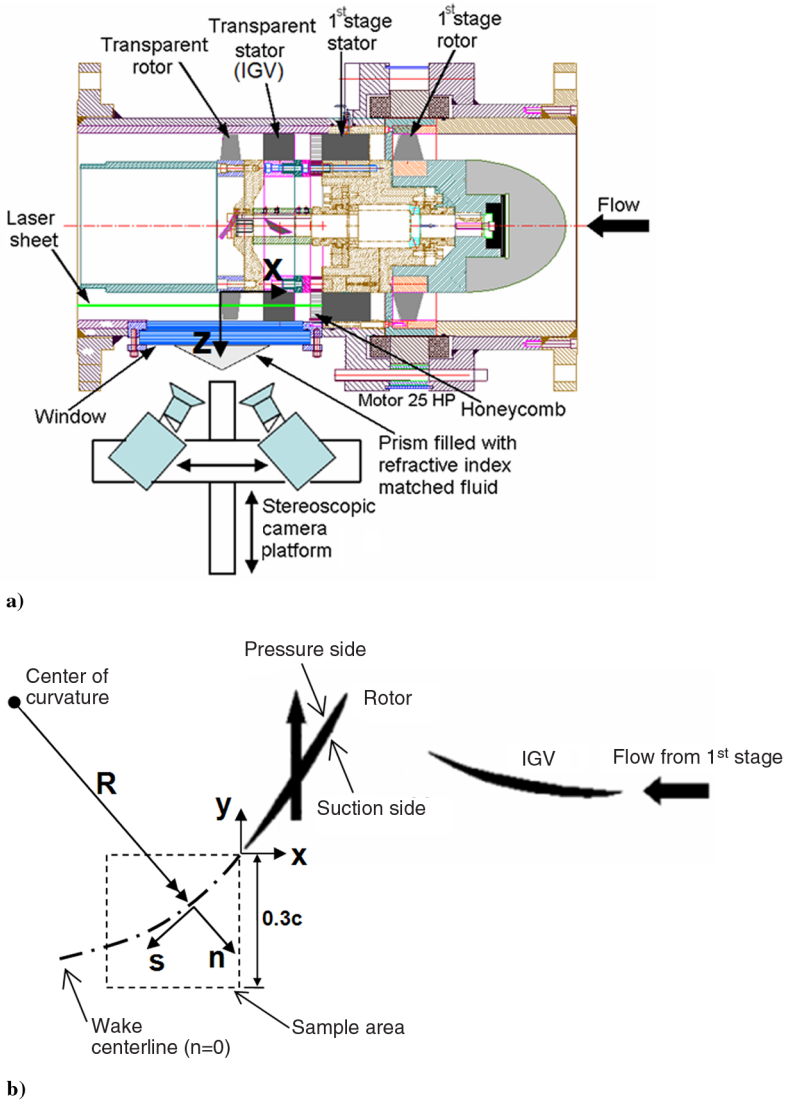

Fig. 3 Schematic representation of a) the test section and the stereoscopic-PIV setup used in the present experiments, and b) IGV blade and rotor blade. Also indicated is the Cartesian coordinate system (x, y, z); coordinate system aligned with the wake centerline (s, n); flow direction and rotor blade displacement direction. The rotor trailing edge is located at $(x/c, y/c) = (s/c, n/c) = (0, 0)$.

$$\overline{U_i}(x, y, z, \phi) = \frac{1}{N}\sum_{k=1}^{N}[u_i(x, y, z, \phi)]_k \tag{1}$$

$$\overline{u_i' u_j'}(x, y, z, \phi) = \frac{1}{N}\sum_{k=1}^{N}\{[u_i(x, y, z, \phi)]_k - \overline{U_i}(x, y, z, \phi)\}\{[u_j(x, y, z, \phi)]_k - \overline{U_j}(x, y, z, \phi)\} \tag{2}$$

where $N = 1000$ is the number of instantaneous realizations, and ϕ is the phase angle. The subscripts i and j take values of 1, 2, and 3, representing the axial ($u_1 = u$), lateral ($u_2 = v$), and radial ($u_3 = w$) velocity components, respectively.

Table 1 Geometric details of the second-stage inlet guide vanes and the rotor blades

	IGV	Rotor
No. of blades	17	12
Chord c, mm	50	50
Span, mm	44.45	43.25
Blade thickness, mm	8.28	7.37 (hub) 5.62 (tip)
Tip clearance, mm	0	1.2
Pitch-to-chord ratio	0.97	1.34
IGV-rotor gap, mm	40	
Hub-to-tip ratio	0.708	0.714

A conservative estimate of the uncertainty in the mean displacement of particle images in each interrogation window is 0.3 pixels, provided that the window contains at least 5–10 particle pairs (Roth et al. [20], Roth and Katz [21]). For the typical displacement between exposures of 20 pixels, the resulting uncertainty in instantaneous velocity is about 1.5%. The uncertainty in the instantaneous out-of-plane vector is estimated to be about 3%. Slip due to the difference between the specific gravity of the particle (1.6) and that of the fluid (1.8) may cause an error of less than 0.2%, that is, much less than other contributors (Sridhar and Katz [22]). Uncertainty related to inflow variations and timing errors is estimated to be less than 0.6%. As discussed in the Appendix, uncertainty in production rate of turbulent kinetic energy is typically less than 10%, and involves uncertainty in the Reynolds stresses and in the phase-averaged velocity gradients.

Data are presented in a reference frame relative to the rotor blade, that is, we subtract the blade speed from the lateral velocity component. Unless otherwise specified, the terms streamwise, cross stream, upstream, and downstream refer to this reference frame. Because part of the data analysis is performed in the (s, n, z) coordinate system, with corresponding velocity components (u_s, u_n, u_z), this coordinate system is defined before proceeding. As shown in Fig. 3b, s follows the wake centerline and n is measured along straight lines perpendicular to s (Bradshaw [23]). We define R as the local radius of curvature of the wake centerline, with R being positive when the local center of curvature is located at $n < 0$ and

negative otherwise. To compute R, the shape of the wake centerline $f(x)$ is approximated as a fourth-order polynomial, least-square fitted through the points with minimum phase-averaged velocity magnitude in the relative frame of reference. Then $R = [1 + (df/dx)^2]^{3/2}/|df/dx^2|$. Note that because the phase-averaged flow at midspan is almost two-dimensional (see next section), torsion of the wake centerline is negligible. As a result, tracing of points with minimum phase-averaged velocity magnitude is done at one specific spanwise plane. We choose the $z/(r_{tip} - r_{hub}) = 0.52$ span plane.

Phase-Averaged Flow and Turbulent Stresses in Cartesian Coordinate System

Figure 4 shows distributions of the phase-averaged velocity and vorticity components in the (x, y, z) system at $z/(r_{tip} - r_{hub}) = 0.52$. The dominant flow features are the rotor wake and flow nonuniformities associated with the wake shed by the upstream IGV blades. Several observations can be readily made.

First, as expected, the rotor wake is characterized by low axial and lateral momentum, the latter in the relative frame of reference (Figs. 4a and 4b). The almost radial velocity component $\overline{W}$ is about an order of magnitude lower than the other two. However, its x and y gradients are not negligible and contribute to make the in-plane vorticity components, especially $\overline{\omega_y}$, comparable to $\overline{\omega_z}$. Contributions to $\overline{\omega_x}$ and $\overline{\omega_y}$ from $\partial\overline{U}/\partial z$ and $\partial\overline{V}/\partial z$ are very small due to the fact that the phase-averaged velocity field at midspan is nearly two-dimensional. To elucidate this point, Fig. 5 shows distributions of the phase-averaged velocity components in a sample (x, z) plane located at $y/c = -0.1$. Clearly, spatial variability in the z direction of the velocity field is small, especially within the near wake. Thus, the dominant velocity components lie in the (x, y) plane, but the vorticity in the near wake is three-dimensional, mostly because of the in-plane (x, y) gradients of $\overline{W}$. In the remainder of the paper, even though data analysis is performed in a single spanwise plane, we make no assumptions on the two-dimensionality, and account for all the terms contributing to turbulence production rate, advection by the phase-averaged flow, and turbulent diffusion.

Second, within the rotor wake $\overline{\omega_z}$, the largest vorticity component (Fig. 4f) is characterized by two distinct layers of opposite signs. Chopped sections of upstream IGV wakes can be seen on both sides of the rotor wake. On the suction side, the IGV-wake segment is located close to the trailing edge, seen as a negative $\overline{\omega_z}$, layer on the upper right-hand corner. On the pressure side, the chopped IGV-wake segment is located on the lower left-hand corner of the sample area. These wake segments are discontinuous due to differences in propagation velocity across the blade. Their signature can also be observed as regions with reduced $-\overline{V_r}$ (the subscript r refers to the relative frame of reference) in Fig. 4b. For further discussion on this IGV-wake structure as it propagates through the rotor passage, one can refer to Soranna et al. [24].

Third, as already discussed in the Introduction, IGV-wake impingement exposes the rotor wake to a nonuniform velocity field. As shown in Fig. 4a, in the $y/c < -0.2$ region, and for this rotor phase, high axial momentum flow associated with the presence of a jet compresses the suction side of the rotor wake, whereas the pressure side is exposed to a low-momentum IGV-wake segment. Compression by the jet, as discussed later, increases the shear velocity gradients on the suction side of the wake. The nonuniform flow also bends the rotor wake toward the pressure side, starting a

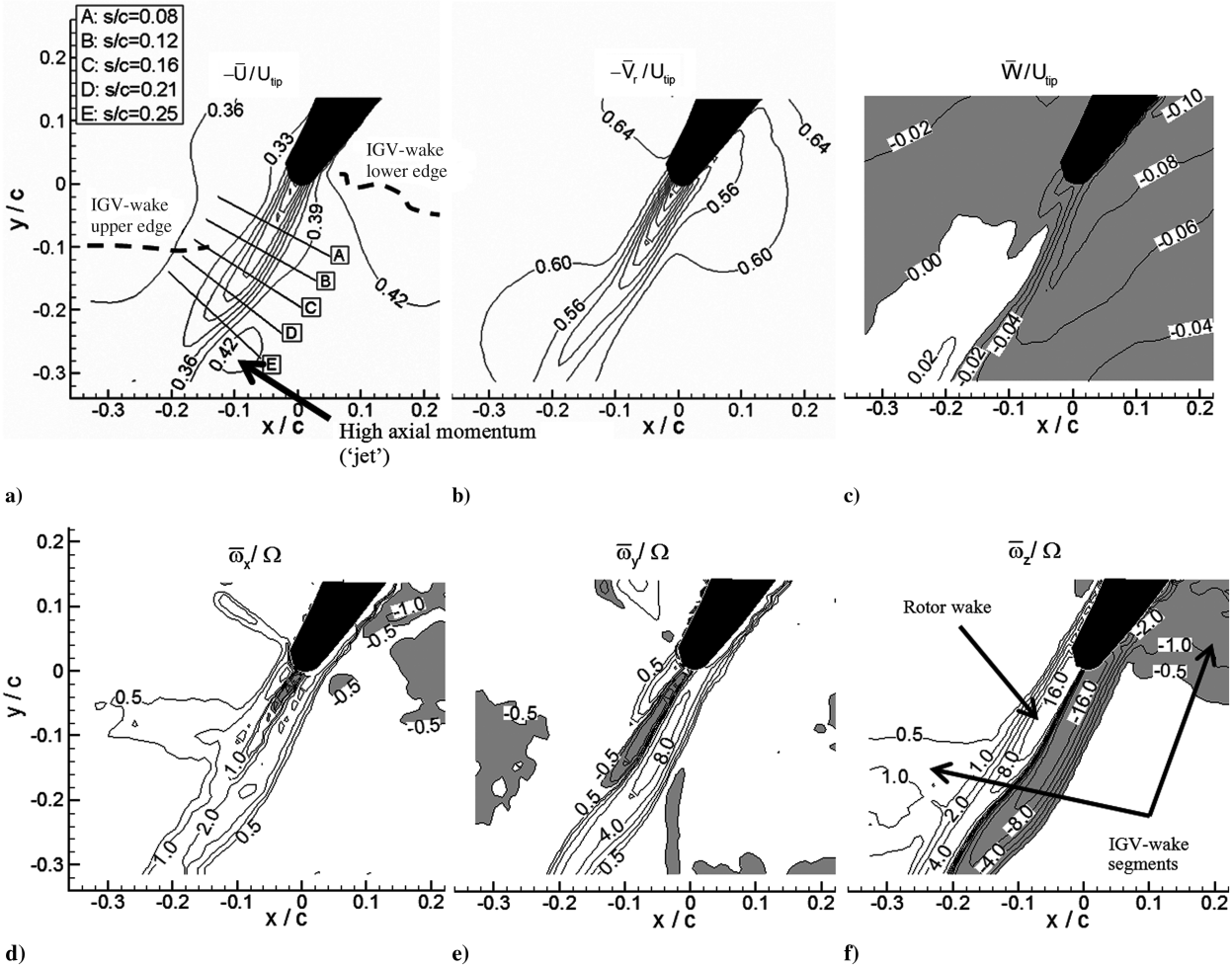

Fig. 4 Phase-averaged velocity components: a) $-\overline{U}$, the contour level increment is 0.03; b) $-\overline{V_r}$, the contour level increment is 0.04; c) $\overline{W}$, the contour level increment is 0.02. $U_{tip} = 8$ m/s. Phase-averaged vorticity components: d) $\overline{\omega_x}$, e) $\overline{\omega_y}$, and f) $\overline{\omega_z}$. The increment between contour levels is by a factor of 2. $\Omega = 52.3$ rad/s. Contour levels corresponding to $\overline{\omega_x} = \overline{\omega_y} = \overline{\omega_z} = 0$ are not shown. For each variable, regions with negative values are shaded gray. In Fig. 4a, dashed lines mark the edges of the IGV-wake segments as identified by the $\overline{\omega_z}/\Omega = \pm 0.05$ contour lines.

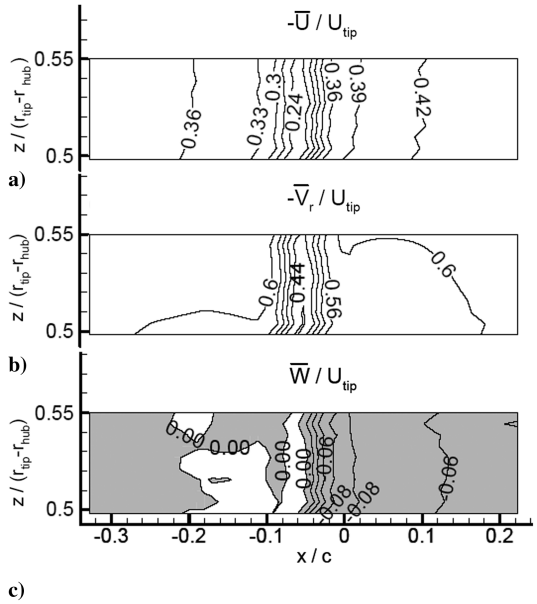

Fig. 5 Phase-averaged velocity components at the $y/c = -0.1$ plane: a) $-\overline{U}$, b) $-\overline{V_r}$, and c) $\overline{W}$. Contour level increments are the same as in Fig. 4.

process that becomes a hot spot at a later phase (Fig. 1). Because of bending, the curvature $(1/R)$ of the wake centerline increases up to $s/c = 0.21$, at which $R/c = 0.41$, then starts decreasing and becomes even negative. Later phases are characterized by more severe wake bending, leading to complete shearing of the wake, as shown in Fig. 1 (Chow et al. [2]).

Finally, the Reynolds stresses clearly deviate from the typical pattern of a decaying wake (Wygnanski et al. [25]). As shown in Fig. 6, $\overline{u'^2}$ increases downstream of the trailing edge up to $s/c \sim 0.21$, with substantially higher levels on the suction side. On the other hand, $\overline{v'^2}$ and $\overline{w'^2}$ decay downstream of the trailing edge, but the decay rates differ across the wake. To provide a quantitative sense of the changes, Fig. 6d compares the distributions of normal Reynolds stress components across the wake at two streamwise locations. Contour plots of normal stresses contain evidence of the chopped IGV-wake segments. The turbulence levels within these segments are lower than those in the rotor wake, and are beyond the scope of the present discussion. The distributions of the shear stresses within the wake (Fig. 7) show that $\overline{u'v'}$ is larger than $\overline{u'w'}$, and they are both much larger than $\overline{v'w'}$. The shear stresses on the suction side are higher than those on the pressure side. The magnitude of $\overline{u'v'}$ decreases monotonically with s on the suction side. On the pressure side, $\overline{u'v'}$ changes sign just below $s/c = 0.08$, but the difference in magnitude of $\overline{u'v'}$ between $s/c = 0.08$ and 0.21 is very small. The values of $\overline{u'w'}$ increase downstream of the trailing edge, whereas the values of $\overline{v'w'}$ decay. The objective of this paper is to identify the causes for these nonuniform and spatially varying trends, which lead to the generation of the turbulent hot spot.

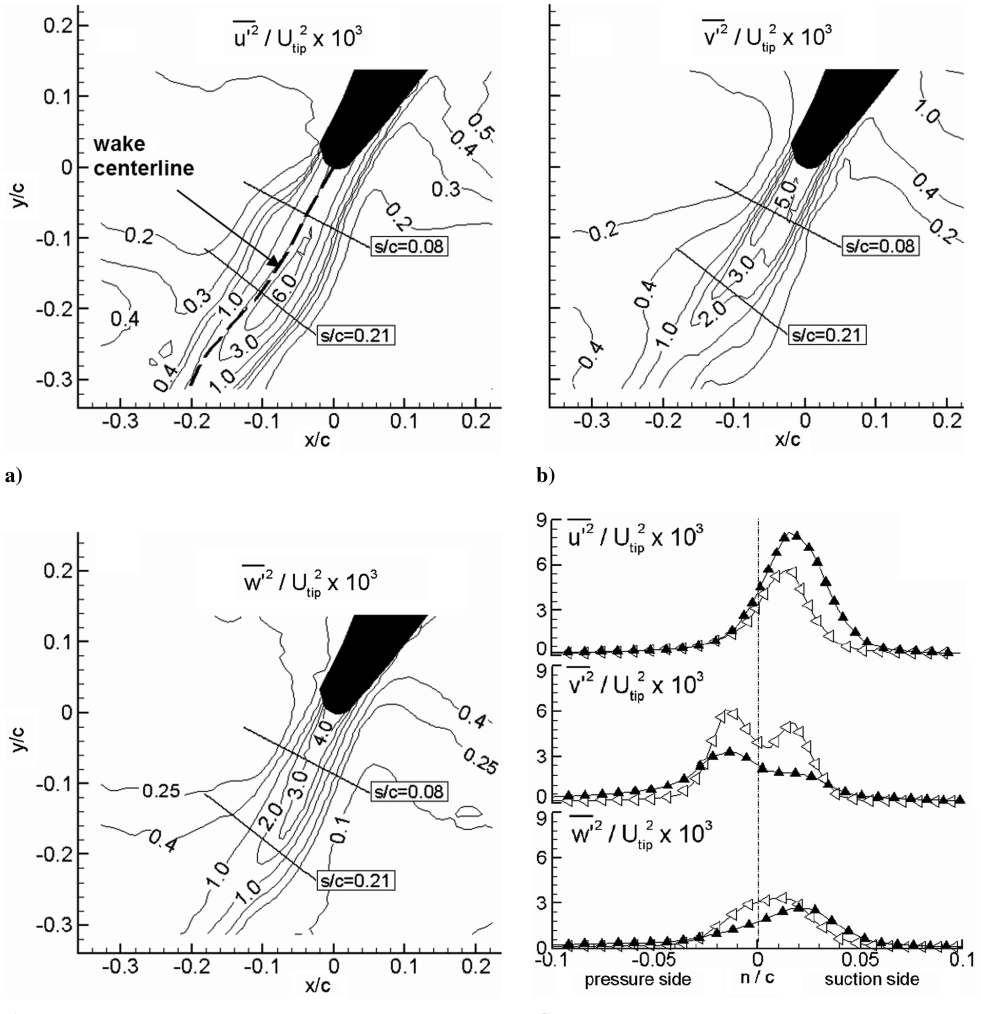

Fig. 6 Normal Reynolds stress components: a–c) distributions of $\overline{u'^2}$, $\overline{v'^2}$, and $\overline{w'^2}$; d) profiles at $s/c = 0.08$ ◁, and $s/c = 0.21$ ▲. Note that the incremental increase in contour lines is nonlinear with values indicated for each line.

Scaling of Velocity and Turbulence Profiles

To fully characterize the rotor wake, we provide, at any station, a suitable estimate of length, velocity, and energy scales. As described in Chow et al. [2], for a wake located in a nonuniform flow, it is impossible to define univocally the wake width and the velocity deficit based on the external velocity. Instead, for each s, we characterize the wake length scale δ_β as the distance from the center of the wake to a point where the local phase-averaged shear strain rate is one-half of the average shear strain rate, that is,

$$\left.\frac{\partial \overline{U_s}}{\partial n}\right|_{n=\delta_\beta} = \frac{1}{2}\frac{\overline{U_s}|_{\delta_\beta} - \overline{U_s}|_0}{\delta_\beta} \tag{3}$$

For clarity, for classical two-dimensional wakes (Wygnanski et al. [25]), $\delta_\beta \approx 1.8\delta$, where δ is the wake half-width. In place of using the external velocity to define a deficit, we use $\overline{U}_\beta$, that is, the velocity at a distance δ_β from the wake center. Evidently, due to the asymmetry of the wake, each side of the wake has its own length and velocity scales (Thomas and Liu [26]). Thus, we calculate $\overline{U}_\beta$ and δ_β for each side separately. Figure 8a shows profiles of the nondimensional velocity defect $[\overline{U}_{\beta,l}(s) - \overline{U_s}(s,n)]/[\overline{U}_{\beta,l}(s) - \overline{U_s}(s,0)]$, where the subscript l refers to the pressure and suction sides, which are scaled independently using the corresponding values of $\overline{U}_\beta$ and δ_β obtained for each side of the wake. Consistent with Chow et al. [2], in the region $|n/\delta_{\beta,l}| < 1$, the profiles collapse onto a single curve. Two different energy scaling parameters are discussed in Chow et al. [2]. The first, $K_1 = [\overline{U}_{\beta,\mathrm{av}}(s) - \overline{U_s}(s,0)]^2$, is based on analysis of fully developed wakes (Wygnanski et al. [25], Pope [27]), where $\overline{U}_{\beta,\mathrm{av}}$ is the average of values of $\overline{U}_\beta$ obtained in the suction and pressure sides. The second one, $K_2 = [\overline{U}_{\beta,\mathrm{av}}(s) - \overline{U_s}(s,0)]\,\mathrm{d}[\overline{U}_{\beta,\mathrm{av}}(s)\,\delta_{\beta,\mathrm{av}}(s)]/\mathrm{d}s$, is based on Thomas and Liu [26], where $\delta_{\beta,\mathrm{av}}$ is the average δ_β in the suction and pressure sides. K_2 is characterized by a slower decay rate than K_1, thus it is more suitable in situations where the decay rate of the turbulence is slower than that of the mean flow, as often occurs in near wakes (e.g., Weygandt and Metha [6], Moser et al. [28]), especially in the presence of favorable pressure gradients (Thomas and Liu [26]) and straining (Rogers [29]). Chow et al. [2] show that the decay rate of the rotor wakes falls between K_1 and K_2. For the present data, the scaling of k with K_2 seems reasonable on the pressure side (Fig. 8b) but fails on the suction side, because the decay rate of k is even slower than that of K_2. Figure 9 shows the variations of $[\overline{U}_\beta(s) - \overline{U_s}(s,0)]$ and δ_β with distance from the trailing edge for each side of the wake. Also shown are distributions of K_1 and K_2 with s. After initial distance, $\delta_\beta \propto s^{0.25}$, that is, the wake grows at a slower rate than that of a plane wake ($\propto s^{0.5}$). The decay of velocity deficit is initially slower than that in a plane wake ($\propto s^{-0.5}$), but in the region subjected to strong external straining, that is, at $s/c > 0.12$, the decay rate increases substantially, especially on the pressure side. The decay rate of K_1 is higher than that of K_2 (Fig. 9c), as expected. For both, the decay rate increases in the region most subjected to external straining. Recall that K_2 is the correct scaling parameter for the pressure side, but not for the suction side.

Contributors to the Spatially Nonuniform Reynolds Stresses: Analysis in the (s, n, z) Coordinate System

In the most general form, the transport equation for the Reynolds stresses is (Pope [27], Lakshminarayana and Reynolds [30])

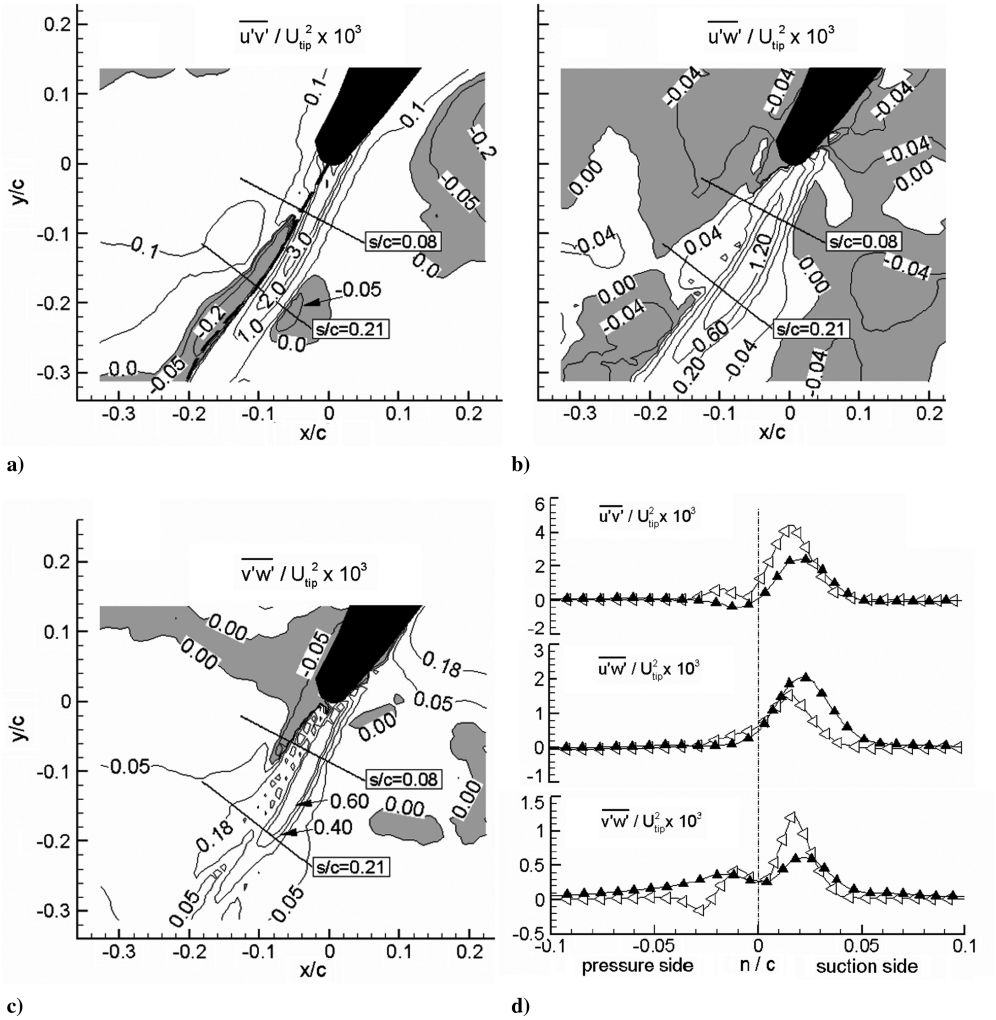

Fig. 7 Reynolds shear stress components: a–c) distributions of $\overline{u'v'}$, $\overline{u'w'}$, and $\overline{v'w'}$; d) profiles at $s/c = 0.08$ ◁, and $s/c = 0.21$ ▲.

$$\frac{\partial}{\partial t}(\overline{u_i' u_j'}) = C_{ij} + P_{ij} + T_{ij} + \Pi_{ij} + V_{ij} - \varepsilon_{ij} \tag{4}$$

where the terms on the right-hand side represent, in order, advection, production rate, turbulent diffusion, velocity-pressure-gradient correlation, viscous diffusion, and dissipation. Note that, in a coordinate system rotating with the rotor blade, an additional term due to Coriolis forces appears on the right-hand side of Eq. (4). As discussed later, its effects are negligible in the wake being examined here. The present PIV experiments do not allow us to calculate the velocity-pressure-gradient correlation tensor, and viscous dissipation is not analyzed due to insufficient resolution to calculate the

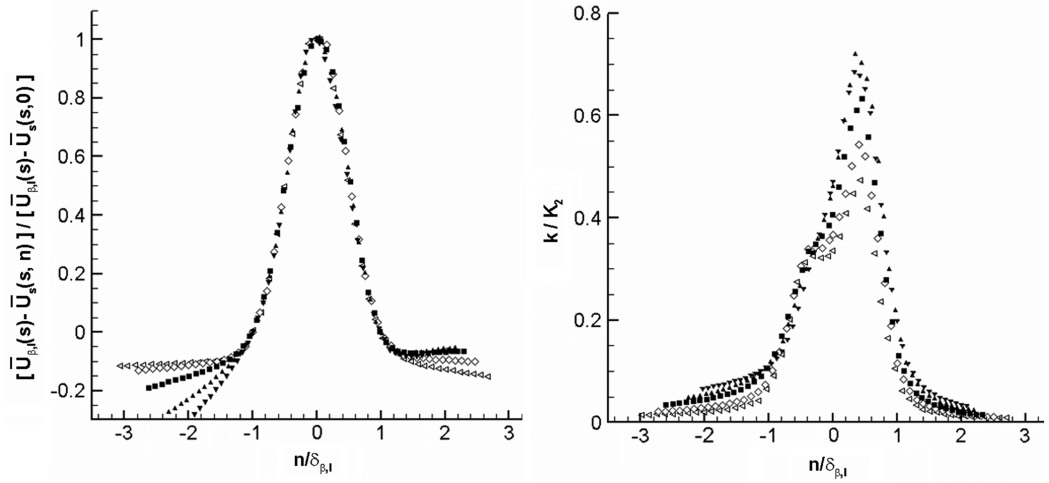

a) b)

Fig. 8 Nondimensional a) phase-averaged velocity defect and b) turbulent kinetic energy profiles at ◁ $s/c = 0.08$, ◇ $s/c = 0.12$, ■ $s/c = 0.16$, ▲ $s/c = 0.21$, ▼ $s/c = 0.25$.

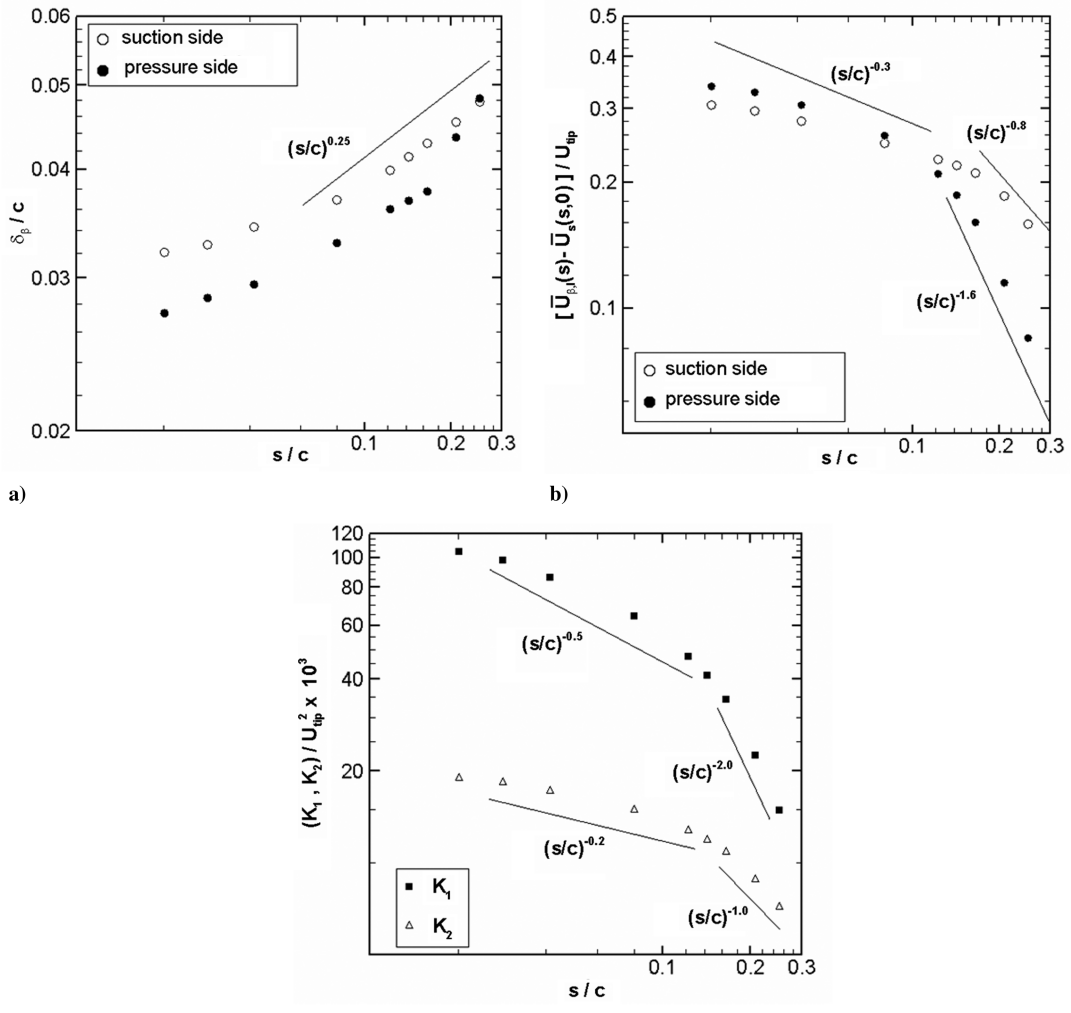

a) b) c)

Fig. 9 Streamwise variation of a) wake length scale, b) wake deficit, and c) $K_1 = [\overline{U}_{\beta,\mathrm{av}}(s) - \overline{U_s}(s,0)]^2$ and $K_2 = [\overline{U}_{\beta,\mathrm{av}}(s) - \overline{U_s}(s,0)]\,\mathrm{d}[\overline{U}_{\beta,\mathrm{av}}(s)\delta_{\beta,\mathrm{ave}}(s)]/\mathrm{d}s$.

dissipation from velocity gradients. The viscous diffusion term is typically small at high Reynolds numbers. The only term that can feed new turbulence into the flow is the production rate, which is given by

$$P_{ij} = -\overline{u_i' u_k'}\frac{\partial \overline{U_j}}{\partial x_k} - \overline{u_j' u_k'}\frac{\partial \overline{U_i}}{\partial x_k} \tag{5}$$

Typically, one would expect an increase in a stress component in a region characterized by high production rate. On the other hand, in regions with low or negative production rate, the corresponding stress is more likely to be reduced due to dissipation or intercomponent transfer. Indeed, as shown in the next section, profiles of Reynolds stresses are consistent with the corresponding production rates.

Following So and Mellor [31], Bradshaw [23], and Weygandt and Metha [6], but including all terms, the transport equations for Reynolds stresses and turbulent kinetic energy in the (s, n, z) coordinate system are

where $h = 1 + n/R$. The underlined terms in Eqs. (6), (7), and (9), are referred to in the literature as "curvature terms" (Nakayama [14], Weygandt and Metha [6]). Because the shear stress changes sign across the wake, the effects of $\overline{u_s' u_n'}(\overline{U_s}/R)$ on the various stress terms are also reversed across the center of the wake. As is evident from Eqs. (6), (7), and (9), the curvature terms decrease $\overline{u_s'^2}$ and increase $\overline{u_n'^2}$ and k on the pressure (inner) side of the wake, and these effects are reversed on the suction (outer) side. Other curvature terms that have asymmetric contribution across the wake can be found in the equation for shear stress. Although the terms $\overline{u_n'^2}(\overline{U_s}/R)$ and $\overline{u_s'^2}(\overline{U_s}/R)$ do not change sign, they have an opposite effect on the shear stress across the wake because the stress changes sign.

In the next section, we examine the available terms in the transport Eqs. (6–9). We focus on the in-plane stress components (but include three-dimensional data) and analyze the effects of production rate, advection, and turbulent diffusion at two stations, $s/c = 0.12$ and 0.21.

$$\begin{aligned}
\frac{\partial}{\partial t}(\overline{u_s'^2}) = &-\left[\frac{1}{h}\overline{U_s}\frac{\partial}{\partial s} + \overline{U_n}\frac{\partial}{\partial n} + \overline{U_z}\frac{\partial}{\partial z}\right](\overline{u_s'^2}) && \Big\} C_{ss}\\
&-\frac{2}{h}\overline{u_s'^2}\left(\frac{\partial \overline{U_s}}{\partial s} + \frac{\overline{U_n}}{R}\right) - 2\overline{u_s' u_n'}\frac{\partial \overline{U_s}}{\partial n} - \underline{\frac{2}{h}\overline{u_s' u_n'}\frac{\overline{U_s}}{R}} - 2\overline{u_s' u_z'}\frac{\partial \overline{U_s}}{\partial z} && \Big\} P_{ss}\\
&-\frac{1}{h}\frac{\partial}{\partial s}(\overline{u_s'^3}) - \frac{1}{h}\frac{\partial}{\partial n}(h\overline{u_n' u_s'^2}) - \frac{2}{h}\frac{\overline{u_s'^2 u_n'}}{R} - \frac{\partial}{\partial z}(\overline{u_z' u_s'^2}) && \Big\} T_{ss}\\
&+\Pi_{ss} + V_{ss} - \varepsilon_{ss} && (6)
\end{aligned}$$

$$\begin{aligned}
\frac{\partial}{\partial t}(\overline{u_n'^2}) = &-\left[\frac{1}{h}\overline{U_s}\frac{\partial}{\partial s} + \overline{U_n}\frac{\partial}{\partial n} + \overline{U_z}\frac{\partial}{\partial z}\right](\overline{u_n'^2}) && \Big\} C_{nn}\\
&-2\overline{u_n'^2}\frac{\partial \overline{U_n}}{\partial n} - \frac{2}{h}\overline{u_s' u_n'}\frac{\partial \overline{U_n}}{\partial s} + \underline{\frac{4}{h}\overline{u_s' u_n'}\frac{\overline{U_s}}{R}} - 2\overline{u_n' u_z'}\frac{\partial \overline{U_n}}{\partial z} && \Big\} P_{nn}\\
&-\frac{1}{h}\frac{\partial}{\partial s}(\overline{u_s' u_n'^2}) - \frac{1}{h}\frac{\partial}{\partial n}(h\overline{u_n'^3}) + \frac{2}{h}\frac{\overline{u_s'^2 u_n'}}{R} - \frac{\partial}{\partial z}(\overline{u_z' u_n'^2}) && \Big\} T_{nn}\\
&+\Pi_{nn} + V_{nn} - \varepsilon_{nn} && (7)
\end{aligned}$$

$$\begin{aligned}
\frac{\partial}{\partial t}(\overline{u_s' u_n'}) = &-\left[\frac{1}{h}\overline{U_s}\frac{\partial}{\partial s} + \overline{U_n}\frac{\partial}{\partial n} + \overline{U_z}\frac{\partial}{\partial z}\right](\overline{u_s' u_n'}) && \Big\} C_{sn}\\
&-\frac{1}{h}\overline{u_s'^2}\left(\frac{\partial \overline{U_n}}{\partial s} - \frac{\overline{U_s}}{R}\right) - \overline{u_n'^2}\frac{\partial \overline{U_s}}{\partial n} + \frac{1}{h}(\overline{u_s'^2} - \overline{u_n'^2})\frac{\overline{U_s}}{R} - \overline{u_s' u_z'}\frac{\partial \overline{U_n}}{\partial z} + \overline{u_s' u_n'}\frac{\partial \overline{U_z}}{\partial z} - \overline{u_n' u_z'}\frac{\partial \overline{U_s}}{\partial z} && \Big\} P_{sn}\\
&-\frac{1}{h}\frac{\partial}{\partial s}(\overline{u_s' u_s' u_n'}) - \frac{\partial}{\partial n}(\overline{u_n' u_s' u_n'}) - \frac{1}{h}\frac{2\overline{u_n' u_s' u_n'} - \overline{u_s'^3}}{R} - \frac{\partial}{\partial z}(\overline{u_z' u_s' u_n'}) && \Big\} T_{sn}\\
&+\Pi_{sn} + V_{sn} - \varepsilon_{sn} && (8)
\end{aligned}$$

$$\begin{aligned}
\frac{\partial}{\partial t}(k) = &-\left[\frac{1}{h}\overline{U_s}\frac{\partial}{\partial s} + \overline{U_n}\frac{\partial}{\partial n} + \overline{U_z}\frac{\partial}{\partial z}\right](k) && \Big\} C\\
&+\left[-\frac{1}{h}\overline{u_s'^2}\left(\frac{\partial \overline{U_s}}{\partial s} + \frac{\overline{U_n}}{R}\right) - \overline{u_n'^2}\frac{\partial \overline{U_n}}{\partial n}\right] - \overline{u_s' u_n'}\left(\frac{\partial \overline{U_s}}{\partial n} + \frac{1}{h}\frac{\partial \overline{U_n}}{\partial s}\right) + \underline{\frac{1}{h}\overline{u_s' u_n'}\frac{\overline{U_s}}{R}} - \left(\overline{u_s' u_z'}\frac{\partial \overline{U_s}}{\partial z} + \overline{u_n' u_z'}\frac{\partial \overline{U_n}}{\partial z}\right)\\
&-\left(\frac{1}{h}\overline{u_s' u_z'}\frac{\partial \overline{U_z}}{\partial s} + \overline{u_n' u_z'}\frac{\partial \overline{U_z}}{\partial n} + \overline{u_z'^2}\frac{\partial \overline{U_z}}{\partial z}\right) && \Big\} P\\
&-\frac{1}{h}\frac{\partial}{\partial s}\left(\overline{u_s' \frac{u_i' u_i'}{2}}\right) - \frac{1}{h}\frac{\partial}{\partial n}\left(h\overline{u_n' \frac{u_i' u_i'}{2}}\right) - \frac{\partial}{\partial z}\left(\overline{u_z' \frac{u_i' u_i'}{2}}\right) && \Big\} T\\
&+\frac{1}{2}(\Pi_{ii} + V_{ii} - \varepsilon_{ii}) && (9)
\end{aligned}$$

Turbulence Production, Advection, and Diffusion Rates in the Rotor Near Wake

The contour plot of production rate [Eq. (9)] presented in Fig. 10a shows that P is highly asymmetric across the rotor wake, with larger values on the suction side. The difference across the wake centerline is particularly high near the $s/c \sim 0.21$ section of the wake, where exposure to the jet occurs. Figure 10b shows that the turbulent kinetic energy is also higher on the suction side of the rotor wake. In subsequent figures, we focus on specific planes to show relationships among terms involved in the Reynolds stress and turbulent kinetic energy evolution equations.

Figure 11 shows several profiles of the Reynolds stresses. Only in-plane components are shown because the others are small. The dominant stress component $\overline{u_s'^2}$ decays with distance from the trailing edge. At any streamwise location, $\overline{u_s'^2}$ is larger on the suction side of the wake, where the peak values decay at a slower rater than on the pressure side. The profiles of $\overline{u_n'^2}$ show increasing trends up to $s/c = 0.21$, after which $\overline{u_n'^2}$ starts decreasing. The shear stress component $\overline{u_s'u_n'}$ is larger, in magnitude, on the suction side. It initially increases with distance on both sides of the wake and then starts decreasing. The decay on the pressure side begins earlier than that on the suction side.

Profiles of P_{ss} and the terms contributing to it, presented in Fig. 12, show that the dominant contributor to this production rate component is $-2\overline{u_s'u_n'}\partial\overline{U_s}/\partial n$ (Figs. 12a and 12b). Thus, its streamwise and cross-stream variations determine the distribution of production rate. As expected, the term $-(2/h)\overline{u_s'^2}(\partial\overline{U_s}/\partial s + \overline{U_n}/R)$ is negative within the wake, but it is much smaller than the shear stress term. The curvature term, as mentioned before, is indeed

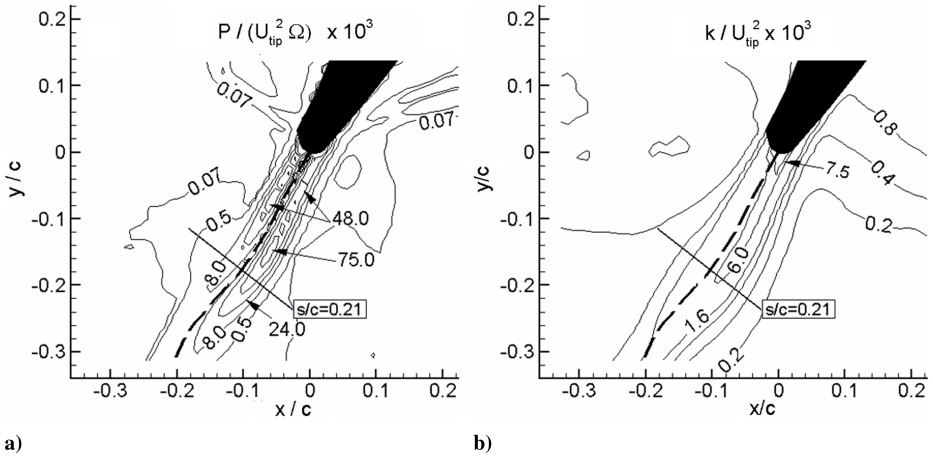

Fig. 10 Distributions in the rotor wake: a) production rate, and b) turbulent kinetic energy.

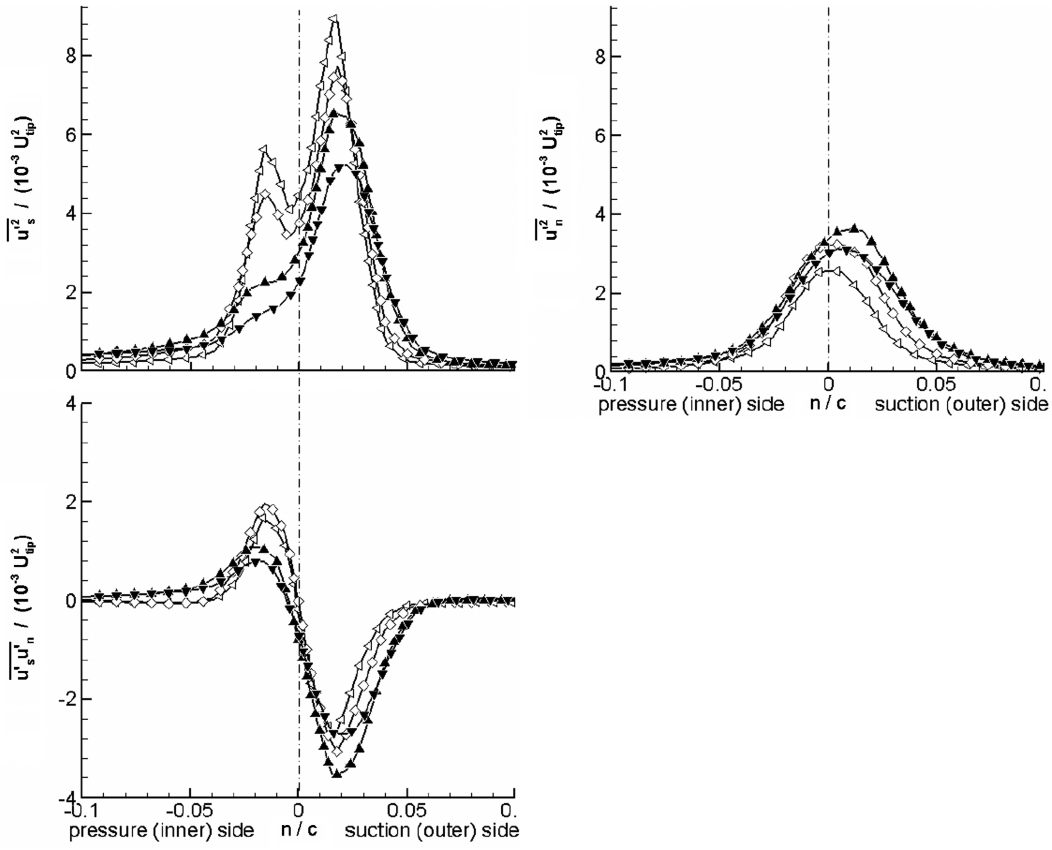

Fig. 11 Profiles of $\overline{u_s'^2}$, $\overline{u_n'^2}$, and $\overline{u_s'u_n'}$ at $\triangleleft$ $s/c = 0.08$, $\diamond$ $s/c = 0.12$, $\blacktriangle$ $s/c = 0.21$, $\blacktriangledown$ $s/c = 0.25$.

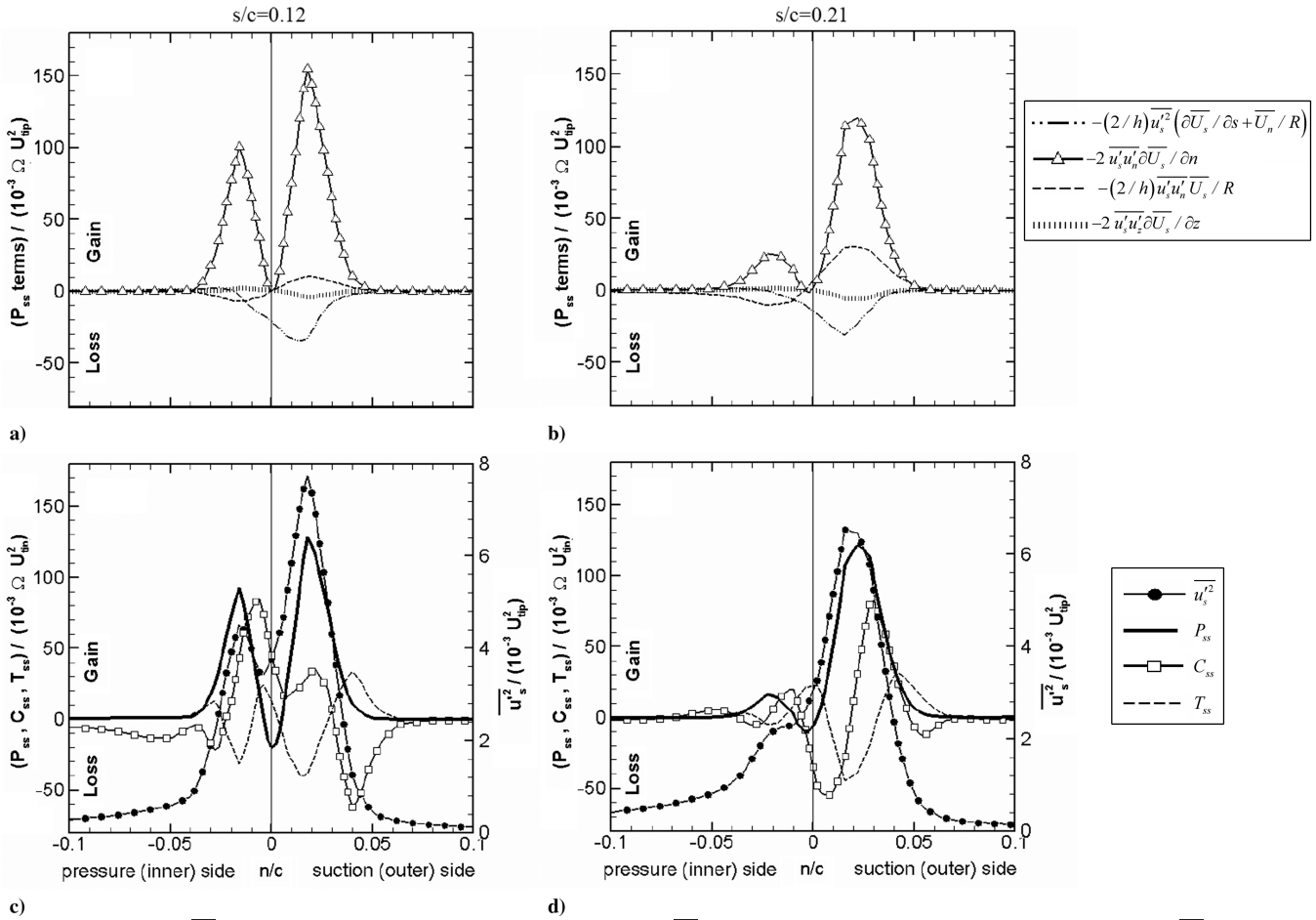

Fig. 12 Budget of $\overline{u_s'^2}$: a–b) terms contributing to P_{ss}, c–d) distribution of $\overline{u_s'^2}$ and profiles of the terms in the transport equation for $\overline{u_s'^2}$ in Eq. (6).

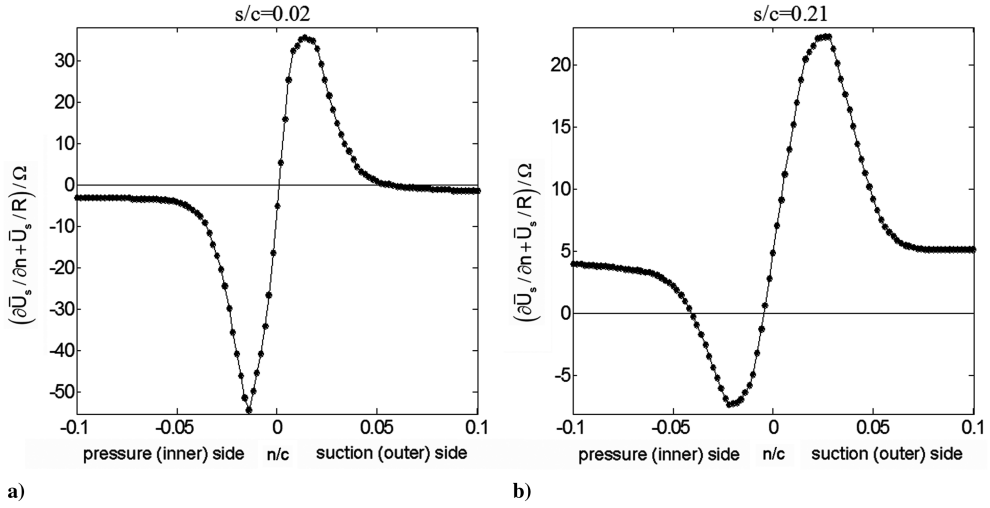

Fig. 13 Profiles of $(\partial\overline{U_s}/\partial n+\overline{U_s}/R)/\Omega$ at $s/c=0.02$ and 0.21.

negative on the pressure (inner) side and positive on the suction (outer) side, but its peak values are only 7 and 25% of $-2\overline{u_s'u_n'}\partial\overline{U_s}/\partial n$ at $s/c=0.12$ and 0.21, respectively. When these terms are combined, at $s/c=0.12$ there are still two P_{ss} peaks on both sides of the wake, but at $s/c=0.21$ most of the production of $\overline{u_s'^2}$ occurs on the suction side. This asymmetry is caused by squeezing/compression of the wake on the suction side by a jet located between two IGV-wake segments, as demonstrated in the Introduction, and shown for this specific phase in Fig. 4. To quantify the effect of compression by the jet, Fig. 13 shows profiles of $(\partial\overline{U_s}/\partial n+\overline{U_s}/R)$ at two stations, $s/c=0.02$ and 0.21. Close to the trailing edge, the magnitude of $(\partial\overline{U_s}/\partial n+\overline{U_s}/R)$ is higher on the pressure side of the wake ($n/c<0$). Further downstream, at $s/c=0.21$, the suction side peak becomes almost three times larger than that in the pressure side. This wake station is located within the region impinged by the jet, which clearly causes the asymmetry in $(\partial\overline{U_s}/\partial n+\overline{U_s}/R)$ and, consequently, production. Agreement between distributions of $\overline{u_s'^2}$ and P_{ss} (Figs. 12c and 12d) indicates that turbulence asymmetries are a direct consequence of the external flow nonuniformities induced by the IGV wakes.

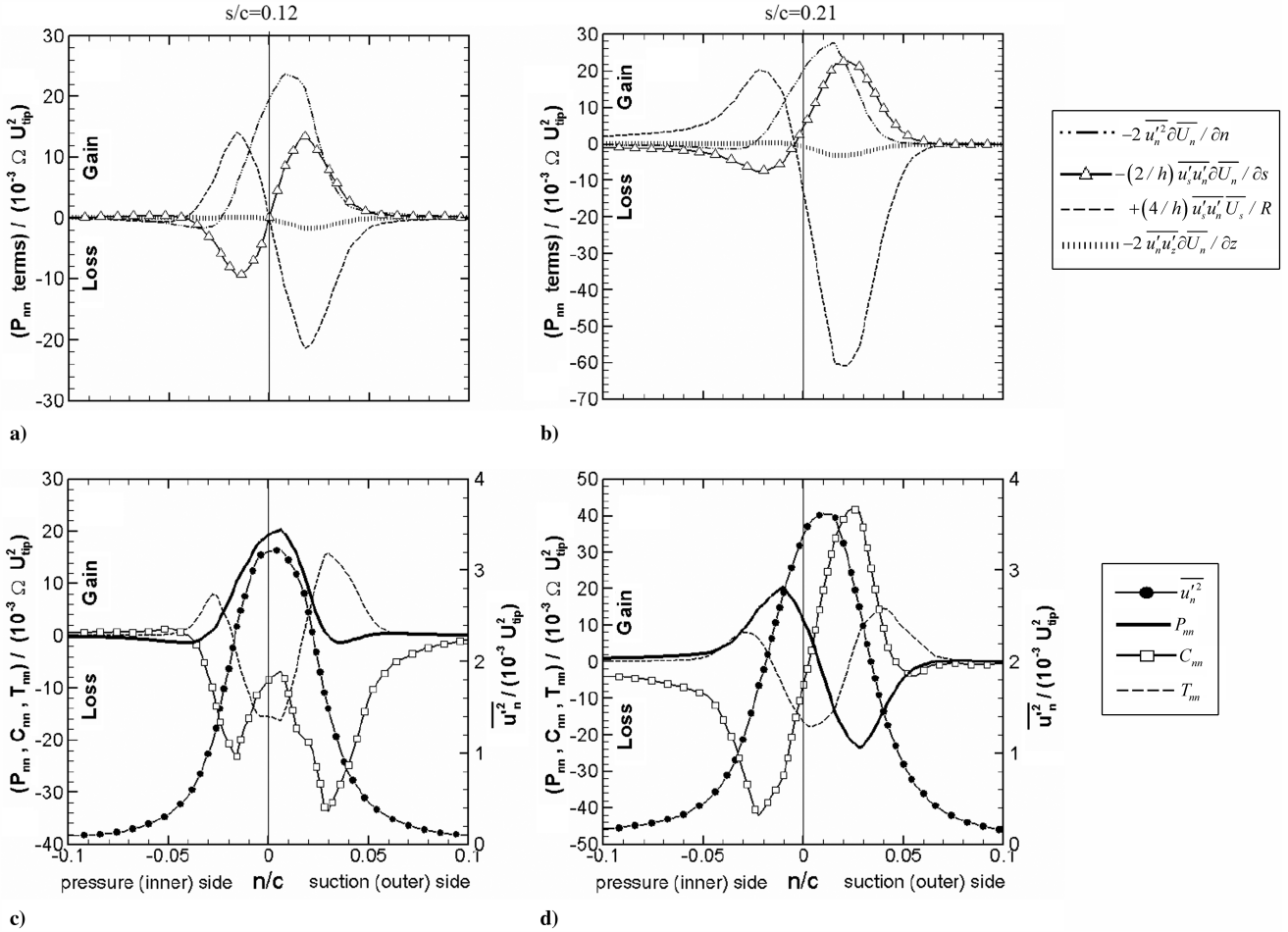

Fig. 14 Budget of $\overline{u_n'^2}$: a–b) terms contributing to P_{nn}, c–d) distribution of $\overline{u_n'^2}$ and profiles of the terms in the transport equation for $\overline{u_n'^2}$ in Eq. (7).

Of the other contributors to $\overline{u_s'^2}$, C_{ss} (Figs. 12c and 12d) varies significantly with s. At $s/c = 0.12$, C_{ss} is dominated by streamwise advection, $-(1/h)\overline{U_s}\partial\overline{u_s'^2}/\partial s$ (not shown), and peaks on the pressure side due to the faster decay of $\overline{u_s'^2}$ there (Fig. 11). At $s/c = 0.21$, cross-stream advection $-\overline{U_n}\partial\overline{u_s'^2}/\partial n$ (also not shown) becomes dominant, and the peak C_{ss} shifts to the suction side. Though smaller than P_{ss}, the effect of T_{ss} is to diffuse the energy away from regions of high production rate. Indeed, T_{ss} typically has negative peaks in regions of maximum production rate. In addition, there are positive peaks of T_{ss} along the boundaries as well as in the middle of the wake. Of the terms contributing to T_{ss}, the largest source is the term $-(1/h)\partial(h\overline{u_n'u_s'^2})/\partial n$ (not shown), that is, the cross-stream transport of $\overline{u_s'^2}$.

At $s/c = 0.12$, three terms contribute to the production of $\overline{u_n'^2}$ (Fig. 14) with different trends but similar magnitudes. Although the peaks of $\overline{u_n'^2}$ and P_{nn} are both located close to the wake center, the peak of P_{nn} is very small (only 15% of P_{ss}), that is, it is not a major source of energy. At $s/c = 0.21$ the curvature term $+(4/h)\overline{u_s'u_n'}\,\overline{U_s}/R$ is larger than and opposes the other two terms, resulting in negative values of P_{nn} on the suction side. The values of P_{nn} are small, and its peak is not located at the same plane as that of $\overline{u_n'^2}$. In fact, the peak in $\overline{u_n'^2}$ shifts to a region where $\overline{u_s'^2}$ is high, suggesting that intercomponent energy transfer may contribute to its value. The diffusion term opposes the production rate at the center of the wake at both stations but has positive peaks along both edges of the wake.

Figure 15 shows the terms contributing to the transport equation for $\overline{u_s'u_n'}$ at $s/c = 0.21$. Data for only one station are presented because the trends are similar. Here, the agreement between distributions of $\overline{u_s'u_n'}$ and P_{sn} is evident. The dominant contributor to P_{sn} is $-\overline{u_n'^2}\partial\overline{U_s}/\partial n$, which is larger, in magnitude, on the suction side due to wake compression by the jet. All the terms related to curvature are small. The large positive advection peak at the middle of the wake is caused by cross-stream transport $-\overline{U_n}\partial\overline{u_s'u_n'}/\partial n$ (not shown). Diffusion opposes the production rate, but also has peaks consistent with the stress sign along the perimeter of the wake.

Because most of the turbulent kinetic energy is associated with streamwise fluctuations, the dominant contributor to the total production rate P (Fig. 16) is the shear production term, of which $-\overline{u_s'u_n'}(\partial\overline{U_s}/\partial n)$ is dominant. Compression of the wake by the jet makes this term highly asymmetric. The peaks of production rate and turbulent kinetic energy on the suction side are closely aligned. The curvature term tends to reduce the production rate on the suction side and increase it on the pressure side. However, its peak magnitude is only ~20% of the shear production term. Because production rate increases with s/c on the suction side (Fig. 10) as the wake is squeezed, the turbulent kinetic energy decays slowly there. Advection peaks to the right of the maximum kinetic energy due to contribution of the terms $-(1/h)\overline{U_s}\partial k/\partial s$ and $-\overline{U_n}\partial k/\partial n$ (not shown). The dominant contributor to diffusion is cross-stream transport, that is, $-(1/h)\partial(h\overline{u_n'u_i'u_i'}/2)/\partial n$ (not shown). As with the components, the turbulent diffusion term opposes the production rate, and has perimeter peaks.

Before concluding this section, it is worthwhile to mention that mechanisms dominating the evolution of turbulence at $s/c > 0.1$ differ from those occurring in the flow around the trailing edge. In another paper by the same authors (Soranna et al. [32]), we show that, at $s/c < 0.1$, the shear production term is strongly affected by IGV-wake-induced changes to the scales of, and turbulence within, the rotor boundary layer.

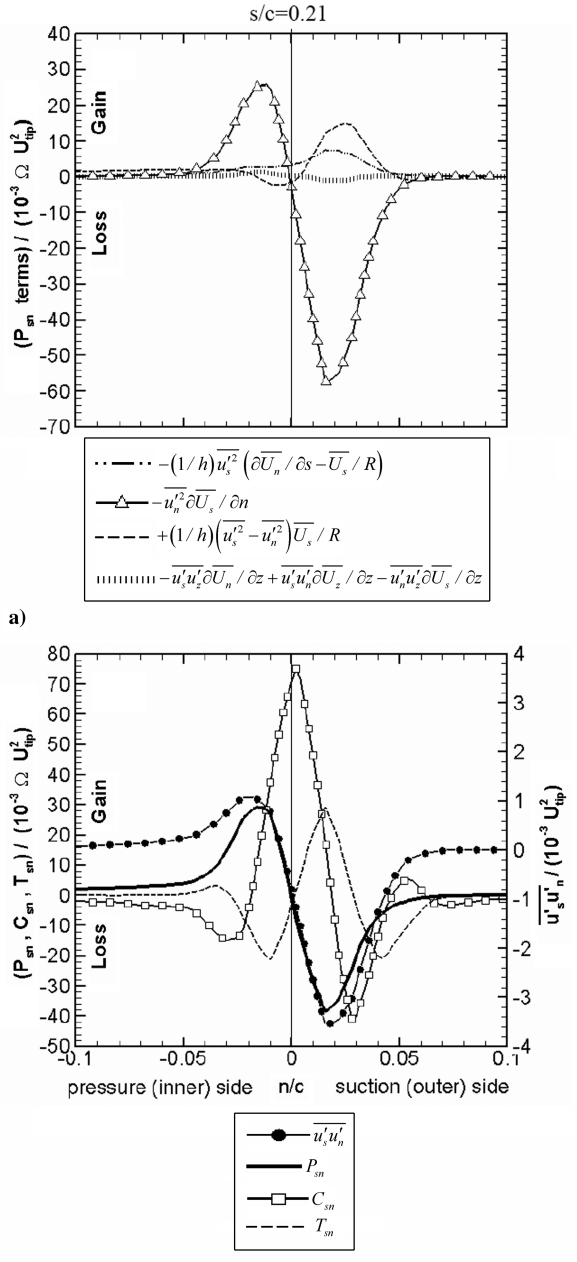

Fig. 15 Budget of $\overline{u_s'u_n'}$: a) terms contributing to P_{sn}, b) distribution of $\overline{u_s'u_n'}$ and profiles of the terms in the transport equation for $\overline{u_s'u_n'}$ in Eq. (8).

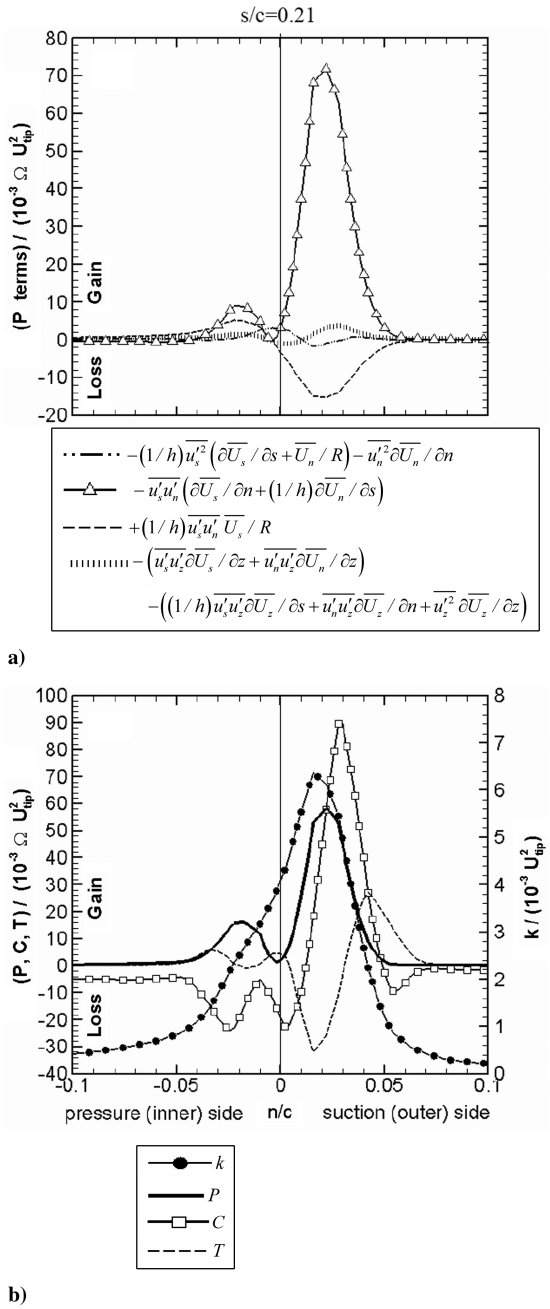

Fig. 16 Budget of k: a) terms contributing to P, b) distribution of k and profiles of the terms in the transport equation for k in Eq. (9).

Contribution of the Coriolis term

Before concluding the analysis of the terms in the transport equation of Reynolds stresses, we provide a few comments on the effects of rotation. The latter can be accounted for by writing Eq. (4) in a coordinate system rotating with the rotor blade. In this system, an additional term due to Coriolis forces appears on the right-hand side of Eq. (4) and is given by (Lakshminarayana and Reynolds [30])

$$-2\Omega^p(\overline{u_i'u_q'}\varepsilon_{jpq}+\overline{u_j'u_q'}\varepsilon_{ipq}) \tag{10}$$

where ε_{jpq} is the permutation tensor and Ω^p is the angular velocity component. To simplify the analysis, we evaluate Eq. (10) in a Cartesian coordinate system rotating about the x axis. For the present turbomachine, $\Omega^p=(-\Omega,0,0)$. As a result, the Coriolis term has no contribution to the evolution of $\overline{u'^2}$, that is, it cannot cause asymmetry of the streamwise velocity fluctuations. It contributes to the evolution of $\overline{u'v'}$ through $-2\Omega\overline{u'w'}$. At $s/c=0.21$, the peak (negative) value of $-2\Omega\overline{u'w'}$ is about 8% of that of the production rate of $\overline{u'v'}$ (not shown). Both peaks occur on the suction side of the wake, at $n/c\sim0.02$, where $\overline{u'v'}$ is maximum. Hence, the effect of this term is minor. In the evolution equations for $\overline{v'^2}$ and $\overline{w'^2}$, Eq. (10) reduces to $-4\Omega\overline{v'w'}$ and $+4\Omega\overline{v'w'}$, respectively, that is, energy is redistributed from $\overline{v'^2}$ to $\overline{w'^2}$. The peak value of $4\Omega\overline{v'w'}$ is also located at $n/c\sim0.02$ and its magnitude is less than 16% of the production rates of $\overline{v'^2}$ and $\overline{w'^2}$ at the same location. Notice that, because the Coriolis term is traceless, it does not contribute to the transport equation of k. Thus, the effect of rotation is not dominant.

Comments on Modeling of Turbulent Diffusion

The diffusion terms in the evolution equation of turbulent kinetic energy have been modeled as $\nabla\cdot(\nu_T\nabla k)$ in numerous studies (Pope [27]), where ν_T is the eddy viscosity. For example, for flow in an axisymmetric sudden expansion, Gould et al. [33] have shown that this model does a respectable job of predicting the diffusion term.

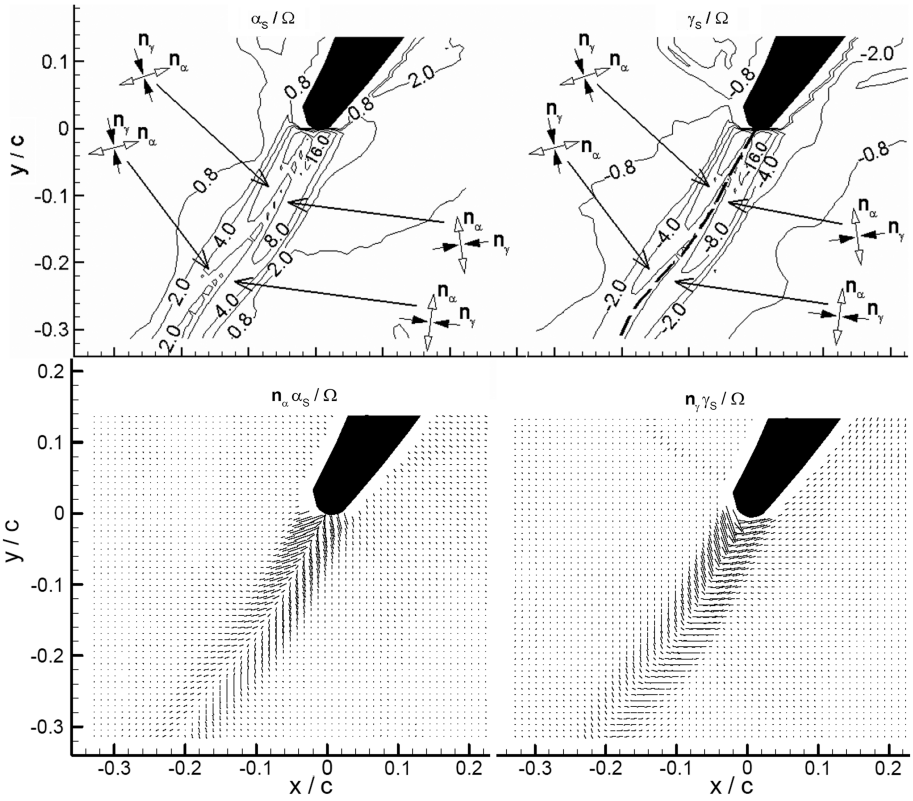

Fig. 17 Components of the principal strain rate tensor. Top: contours of extensive and compressive principal strain rates. Bottom: projections of the principal directions of extension and compression onto the (x, y) plane. The length of each line is proportional to the local magnitude of the strain rate component.

Thus, it could be of interest to compare the distribution of T to that of $\nabla \cdot (\nu_T \nabla k)$. Starting from the constitutive relationship

$$-\overline{u_i' u_j'} = 2\nu_T \overline{S_{ij}} - 2/3 k \delta_{ij} \tag{11}$$

where $\overline{S_{ij}}$ is the phase-averaged strain rate tensor and δ_{ij} is the Kronecker delta, the eddy viscosity is estimated using

$$\nu_T = -\frac{P}{2\overline{S_{ij}}\,\overline{S_{ji}}} \tag{12}$$

that is, by matching the modeled and actual production rates (Laurence [34]). Hence, ν_T, obtained by substituting the "exact" (experimental) data into Eq. (12), is the eddy viscosity that should be matched by models. Because we do not measure dissipation rate, we cannot compare the measured ν_T to k-ε type models.

To simplify the analysis, the product $\overline{S_{ij}}\,\overline{S_{ji}}$ in Eq. (12) is calculated using the eigenvalues of the strain rate tensor α_s, β_s, and γ_s, the most extensive, intermediate, and most compressive principal strain rate components, respectively. Substituting them into Eq. (12), yields

$$\nu_T = -\frac{P}{2\left(\alpha_s^2 + \gamma_s^2 + \beta_s^2\right)} \tag{13}$$

Before evaluating the model, let us comment on distributions of α_s and γ_s, which are shown in Fig. 17. We do not present β_s because its magnitude is more than an order of magnitude smaller than those of α_s and γ_s. Both principal strain rate components decay with distance from the trailing edge, but their decay rate on the suction side is slower, due to wake bending and compression. Figure 17 also shows the in-plane projections of the eigendirections of compression and

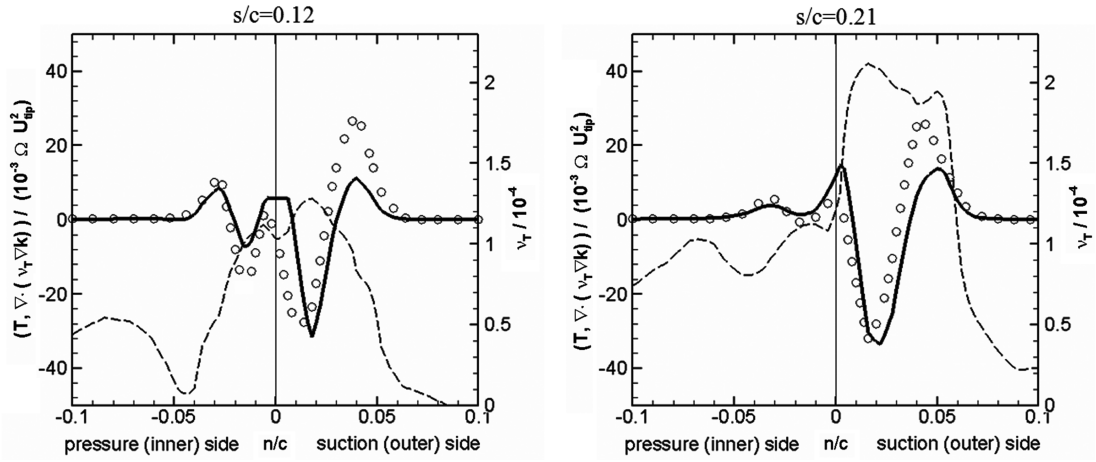

Fig. 18 Terms involved in modeling of turbulent diffusion. Dashed line: distributions of eddy-viscosity across the rotor wake [Eq. (13)]; circles: measured turbulent kinetic energy diffusion; solid line: $\nabla \cdot (\nu_T \nabla k)$.

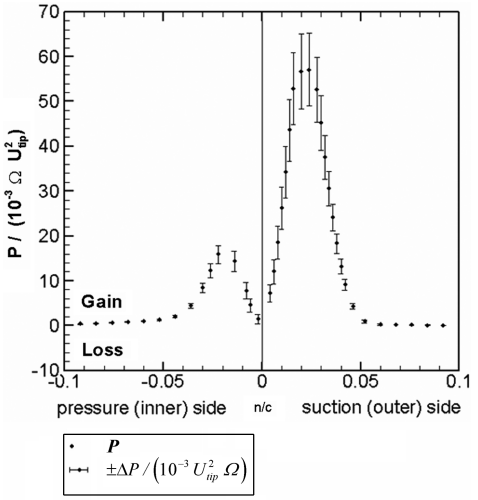

Fig. A1 Error bars indicating uncertainty in turbulent kinetic energy production rate at $s/c = 0.21$.

extension, respectively, $\boldsymbol{n}_\gamma$ and $\boldsymbol{n}_\alpha$, multiplied by the magnitude of the corresponding principal strain rate component. Notice that the eigendirections of compression and extension deviate from their in-plane projections by less than 30 deg. Because of wake bending, $\boldsymbol{n}_\gamma$ and $\boldsymbol{n}_\alpha$ vary with s, and corresponding components across the wake are not perpendicular to each other. Analysis of the production tensor components in coordinate systems aligned with the principal-strain directions (not shown) reveals that most of the production occurs along the compressive eigendirections, with larger values on the suction side of the wake. Accordingly, the velocity fluctuations along $\boldsymbol{n}_\gamma$ are larger than those along $\boldsymbol{n}_\alpha$, and their peak values are located on the suction side. Clearly, the two sides of the wake experience considerably different straining histories, both in direction and magnitude, which affect the spatial distribution of turbulence production. Thus, one should expect to see substantial variations in the distributions of eddy viscosity.

Figure 18 presents the profiles of ν_T at $s/c = 0.12$ and 0.21, as obtained by Eq. (13). Clearly, the magnitudes of ν_T vary substantially, peaking in the middle of the wake at $s/c = 0.12$ and on the suction side at $s/c = 0.21$. Our values are similar in range of magnitudes to those obtained by Hah and Lakshminarayana [7] in their study of the wake of an airfoil at incidence. They also observe that ν_T is low at the perimeter of the wake and peaks in the middle. The eddy viscosity increases with s, that is, the turbulent stresses decay at a slower pace compared to the strain rate. The trends of $\nabla \cdot (\nu_T \nabla k)$, also shown in Fig. 18, agree with the measured values of T in the regions of peak production rate (e.g., $n/c = 0.02$ at $s/c = 0.21$). However, the model underpredicts the peaks of T along the perimeter of the wake, for example, at $n/c = 0.04$ at $s/c = 0.21$. Recall that these peaks are caused by $-(1/h)\partial(h\overline{u'_n u'_i u'_i}/2)/\partial n$, that is, by cross-stream diffusion of turbulence, and apparently the cross-stream decay of k is not fast enough to model this process. Furthermore, the model overpredicts the local peak of T around the wake center at both stations, but especially at $s/c = 0.21$, where overprediction is caused by large cross-stream gradients of ν_T.

Conclusions

Stereoscopic PIV measurements performed in the near wake of a rotor blade located behind a row of inlet guide vanes enable us to investigate the process leading to generation of turbulent hot spots within the rotor wake (Figs. 1 and 2). These spots persist over a substantial fraction of the blade and their signatures can be detected far downstream. We demonstrate that the rotor near wake is exposed to alternating regions with high axial momentum (jet) and wakes of the upstream IGV blades. In the jet regions, the wake is bent and compressed. On the suction side of the wake, compression by the jet enhances the shear velocity gradients ($\partial \overline{U_s}/\partial n$) and, with them, the shear production term, the dominant source of turbulence. Consequently, the Reynolds stresses and turbulent kinetic energy profiles become asymmetric across the rotor wake, with peak values located on the suction side, coinciding with the region of peak production. The effects of streamlines curvature and rotation on the evolution of turbulent stresses are not dominant. As data of later phases show, the process of wake bending and compression by the jet continues as the rotor wake propagates away from the blade, eventually forming distinct kinks containing regions with high turbulence, which we have coined turbulent hot spots (Chow et al. [1]).

The paper provides also distributions of turbulence advection by the phase-averaged flow along with the turbulent diffusion components. The diffusion terms consistently have peaks that oppose the production rate peaks. However, they also have maxima along the perimeter of the wake. We also compare the distribution of diffusion of turbulent kinetic energy to $\nabla \cdot (\nu_T \nabla k)$, a common expression used for modeling the diffusion. The model predicts the diffusion peak that opposes the production rate quite well, but underpredicts the diffusion along the perimeter of the wake and overpredicts it near the wake center.

Appendix A: Uncertainty in Production Rate

An uncertainty analysis is performed to quantify the accuracy of the computed production rate. The uncertainty in P can be estimated as

$$\Delta P = [\partial \overline{U_i}/\partial x_j \partial \overline{U_i}/\partial x_j (\Delta \overline{u'_i u'_j})^2 + \overline{u'_i u'_j}\,\overline{u'_i u'_j}(\Delta \partial \overline{U_i}/\partial x_j)^2]^{1/2} \tag{A1}$$

(Ozcan et al. [35]), where $\Delta \overline{u'_i u'_j}$ and $\Delta \partial \overline{U_i}/\partial x_j$ are uncertainties in $\overline{u'_i u'_j}$ and $\partial \overline{U_i}/\partial x_j$, respectively. The first is estimated as

$$\Delta \overline{u'_i u'_j} = 1.96[(1 + R_{ij}^2)\overline{u_i'^2}\,\overline{u_j'^2}/N]^{1/2} \tag{A2}$$

(Benedict and Gould [36]), where $R_{ij} = \overline{u'_i u'_j}/[\overline{u_i'^2}\,\overline{u_j'^2}]^{1/2}$ is the correlation coefficient and N is the ensemble size. The second is mostly associated with truncation error of the central difference scheme and is given by

$$\Delta \partial \overline{U_i}/\partial x_j = -(1/6)(\partial^3 \overline{U_i}/\partial x_j^3)\Delta x_j^2 \tag{A3}$$

(no summation over j), where Δx_j is the separation between PIV vectors along the jth direction. The third-order partial derivative is evaluated using a central difference scheme (Ozcan et al. [35]). Figure A1 presents a sample distribution of uncertainty in production rate at $s/c = 0.21$, indicated by the error bars of normalized ΔP. The maximum uncertainty is 14.4% of the local production rate and occurs at the location of maximum P ($n/c \sim 0.02$).

Acknowledgments

This project is sponsored in part by the U.S. Office of Naval Research, under grant number N00014-03-1-0145, managed by Ki-Han Kim, and in part by the U.S. Air Force Office of Scientific Research, under grant number FA9550-04-1-0019, managed by Rhett Jefferies. We would like to thank Yury Ronzhes and Stephen King for their contribution to the construction and maintenance of the facility, and Yu-Tai Lee (Naval Surface Warfare Center, Carderock) for designing the blades.

References

[1] Chow, Y-C., Uzol, O., and Katz, J., "Flow Non-Uniformities and Turbulent 'Hot Spots' Due to Wake-Blade and Wake-Wake Interactions in a Multistage Turbomachine," *Journal of Turbomachinery*, Vol. 124, No. 4, 2002, pp. 553–563. doi:10.1115/1.1509078

[2] Chow, Y-C., Uzol, O., Katz, J., and Meneveau, C., "Decomposition of the Spatially Filtered and Ensemble Averaged Kinetic Energy, the Associated Fluxes and Scaling Trends in a Rotor Wake," *Physics of Fluids*, Vol. 17, No. 8, 2005, pp. 085102-1– 85102-20. doi:10.1063/1.1990206

[3] Kurosaka, M., Gertz, J. B., Graham, J. E., Goodman, J. R., Sundaram,

P., Riner, W. C., Kuroda, H., and Hankey, W. L., "Energy Separation in a Vortex Street," *Journal of Fluid Mechanics*, Vol. 178, 1987, pp. 1–29.
[4] Sieverding, C. H., Ottolia, D., Bagnera, C., Cimadoro, A., Brouckaert, J. F., and Desse, J. M., "Unsteady Turbine Blade Wake Characteristics," *Journal of Turbomachinery*, Vol. 126, No. 4, 2004, pp. 551–559. doi:10.1115/1.1737783
[5] Eckert, E. R. G., and Weise, W., "Messungen der Temperaturverteilung auf der Oberfläche schnell angeströmter unbeheizter Körper," *Forschung im Ingenieurwesen*, Vol. 13, No. 6, 1942, pp. 246–254. doi:10.1007/BF02585343
[6] Weygandt, J. H., and Metha, R. D., "Three-Dimensional Structure of Straight and Curved Plane Wakes," *Journal of Fluid Mechanics*, Vol. 282, 1995, pp. 279–311. doi:10.1017/S0022112095000140
[7] Hah, C., and Lakshminarayana, B., "Measurements and Prediction of Mean Velocity and Turbulence Structure in the near Wake of an Airfoil," *Journal of Fluid Mechanics*, Vol. 115, 1982, pp. 251–282. doi:10.1017/S0022112082000743
[8] Raj, R., and Lakshminarayana, B., "Characteristics of the Wake Behind a Cascade of Airfoils," *Journal of Fluid Mechanics*, Vol. 61, 1973, pp. 707–730. doi:10.1017/S002211207300090X
[9] Ramjee, V., Tulapurkara, E. G., and Rajasekar, R., "Development of Airfoil Wake in a Longitudinally Curved Stream,"*AIAA Journal*, Vol. 26, No. 8, 1988, pp. 948–953. doi:10.2514/3.9995
[10] Koyama, H., "Effects of Streamline Curvature on Laminar and Turbulent Wakes," *Proceedings of Fourth Symposium on Turbulent Shear Flows*, Tokyo Electrical Engineering Univ., Tokyo, Sept. 1983, pp. 6.32–6.37.
[11] Ramjee, V., and Neelakandan, D., "Development of Wake of a Rectangular Cylinder in a Curved Stream," *Experiments in Fluids*, Vol. 7, No. 6, 1989, pp. 395–399. doi:10.1007/BF00193421
[12] Schobeiri, M. T., Pappu, K., and John, J., "Theoretical and Experimental Study of Development of Two-Dimensional Steady and Unsteady Wakes Within Curved Channels," *Journal of Fluids Engineering*, Vol. 117, No. 4, 1995, pp. 593–598. doi:10.1115/1.2817308
[13] Savill, A. M., "Turbulent Structure of a Highly Curved Two-Dimensional Wake," *Proceedings of the IUTAM Symposium on Complex Turbulent Flows*, edited by R. Dumas, and F. Fulachier, Springer, Berlin, Aug. 1983, pp. 185–197.
[14] Nakayama, A., "Curvature and Pressure-Gradient Effects on a Small-Defect Wake," *Journal of Fluid Mechanics*, Vol. 175, 1987, pp. 215–246. doi:10.1017/S0022112087000375
[15] John, J., and Schobeiri, M. T., "Development of a Two-Dimensional Turbulent Wake in a Curved Channel with a Positive Streamwise Pressure Gradient," *Journal of Fluids Engineering*, Vol. 118, No. 2, 1996, pp. 292–299. doi:10.1115/1.2817376
[16] Starke, A. R., Henkes, R. A. W. M., and Tummers, M. J., "Effects of Curvature and Pressure Gradient on a Turbulent near Wake," *Experimental Thermal and Fluid Science*, Vol. 19, No. 1, 1999, pp. 49–56. doi:10.1016/S0894-1777(99)00009-6
[17] Uzol, O., Chow, Y-C., Katz, J., and Meneveau, C., "Unobstructed PIV Measurements Within an Axial Turbo-Pump Using Liquid and Blades with Matched Refractive Indices," *Experiments in Fluids*, Vol. 33, No. 6, 2002, pp. 909–919.
[18] Uzol, O., Chow, Y-C., Katz, J., and Meneveau, C., "Experimental Investigation of Unsteady Flow Field Within a Two Stage Axial Turbomachine Using Particle Image Velocimetry," *Journal of Turbomachinery*, Vol. 124, No. 4, 2002. pp. 542–552. doi:10.1115/1.1509077
[19] Prasad, A. K., and Jensen, K., "Scheimpflug Stereocamera for Particle Image Velocimetry in Liquid Flows," *Applied Optics*, Vol. 34, No. 30, 1995, pp. 7092–7099.
[20] Roth, G. I., Mascenik, D. T., and Katz, J., "Measurements of the Flow Structure and Turbulence Within a Ship Bow Wave," *Physics of Fluids*, Vol. 11, No. 11, 1999, pp. 3512–3523. doi:10.1063/1.870209
[21] Roth, G. I., and Katz, J., "Five Techniques for Increasing the Speed and Accuracy of PIV Interrogation," *Measurement Science and Technology*, Vol. 12, No. 3, 2001, pp. 238–245. doi:10.1088/0957-0233/12/3/302
[22] Sridhar, G., and Katz, J., "Drag and Lift Forces on Microscopic Bubbles Entrained by a Vortex," *Physics of Fluids*, Vol. 7, No. 2, 1995, pp. 389–399. doi:10.1063/1.868637
[23] Bradshaw, P., "Effects of Streamline Curvature on Turbulent Flow," AGARDograph 169, Aug. 1973.
[24] Soranna, F., Chow, Y.-C., Uzol, O., and Katz, J., "Effect of Inlet Guide Vanes Wake Impingement on the Flow Structure and Turbulence Around a Rotor Blade," *Journal of Turbomachinery*, Vol. 128, No. 1, 2006, pp. 82–95. doi:10.1115/1.2098755
[25] Wygnanski, I., Champagne, F., and Marsali, B., "On the Large-Scale Structures in Two-Dimensional, Small-Deficit, Turbulent Wakes," *Journal of Fluid Mechanics*, Vol. 168, 1986, pp. 31–71. doi:10.1017/S0022112086000289
[26] Thomas, F. O., and Liu, X., "Experimental Investigation of Symmetric and Asymmetric Turbulent Wake Development in Pressure Gradient," *Physics of Fluids*, Vol. 16, No. 5, 2004, pp. 1725–1745. doi:10.1063/1.1687410
[27] Pope, S. B., *Turbulent Flows*, Cambridge Univ. Press, Cambridge, England, U.K., 2000.
[28] Moser, R. D., Rogers, M. M., and Ewing, W., "Self-Similarity of Time-Evolving Plane Wakes," *Journal of Fluid Mechanics*, Vol. 367, 1998, pp. 255–289. doi:10.1017/S0022112098001426
[29] Rogers, M., "Evolution of Strained Turbulent Plane Wakes," *Journal of Fluid Mechanics*, Vol. 463, 2002, pp. 53–120. doi:10.1017/S0022112002008686
[30] Lakshminarayana, B., and Reynolds, B., "Turbulence Characteristics in the Near Wake of a Compressor Rotor Blade," *AIAA Journal*, Vol. 18, No. 11, 1980, pp. 1354–1362. doi:10.2514/3.50891
[31] So, R. M. C., and Mellor, G. L., "Experimental Investigation of Turbulent Boundary Layers Along Curved Surfaces," NASA CR-1940, 1972.
[32] Soranna, F., Chow, Y. C., Uzol, O., and Katz, J., "Effects of IGV-Wake Impingement on the Boundary Layer and the Near-Wake of a Rotor Blade," American Society of Mechanical Engineers International Gas Turbine Inst. GT 2008-50598, June 2008.
[33] Gould, R. D., Stevenson, W. H., and Doyle, T., "Investigation of Turbulent Transport in an Axisymmetric Sudden Expansion," *AIAA Journal*, Vol. 28, No. 2, 1990, pp. 276–283. doi:10.2514/3.10385
[34] Laurence, D., *2002 Applications of Reynolds Averaged Navier Stokes Equations to Industrial Flows*, von Kármán Institute Lecture Series: Introduction to Turbulence Modeling, von Kármán Inst. for Fluid Dynamics, Sint-Genesius-Rode, Belgium, 2002.
[35] Ozcan, O., Meyer, K. E., and Larsen, P. S., "Measurement of Mean Rotation and Strain-Rate Tensors by Using Stereoscopic PIV," *Experiments in Fluids*, Vol. 39, No. 4, 2005, pp. 771–783. doi:10.1007/s00348-005-0010-z
[36] Benedict, L. H., and Gould, R. D., "Towards Better Uncertainty Estimates for Turbulence Statistics," *Experiments in Fluids*, Vol. 22, No. 2, 1996, pp. 129–136. doi:10.1007/s003480050030

K. Ghia
Associate Editor